

1 **TANAGER: Design and Validation of an Automated Spectrogoniometer for Bidirectional**  
2 **Reflectance Studies of Natural Rock Surfaces**

3 Melissa Rice, Kristiana Lapo, Kathleen Hoza, Ed Cloutis, Mike Kraft, Sean Mulcahy, Dan  
4 Applin

5  
6 **Abstract**

7 Laboratory measurements of reflectance spectra of rocks and minerals at multiple  
8 viewing geometries are important for interpreting spacecraft data of planetary surfaces.  
9 However, efficiently acquiring such measurements is challenging, as it requires a custom  
10 goniometer that can accommodate multiple, bulky samples beneath a movable light source and  
11 detector. Most spectrogoniometric laboratory work to date has focused on mineral mixtures and  
12 particulates, yet it is also critical to characterize natural rock surfaces to understand the influence  
13 of texture and alteration. We designed the Three-Axis N-sample Automated Goniometer for  
14 Evaluating Reflectance (TANAGER) specifically to rapidly acquire spectra of natural rock  
15 surfaces across the full scattering hemisphere. TANAGER has its light source and the  
16 spectrometer's fiber optic mounted on motorized rotating and tilting arcs, with a rotating azimuth  
17 stage and six-position sample tray, all of which are fully motorized and integrated with a  
18 Malvern PanAnalytical ASD FieldSpec4 Hi-Res reflectance spectrometer. Using well-  
19 characterized color calibration targets, we have validated the accuracy and repeatability of  
20 TANAGER spectra. We also confirm that the system introduces no discernable noise or artifacts.  
21 All design schematics and control software for TANAGER are open-source and available for use  
22 and modification by the larger scientific community.

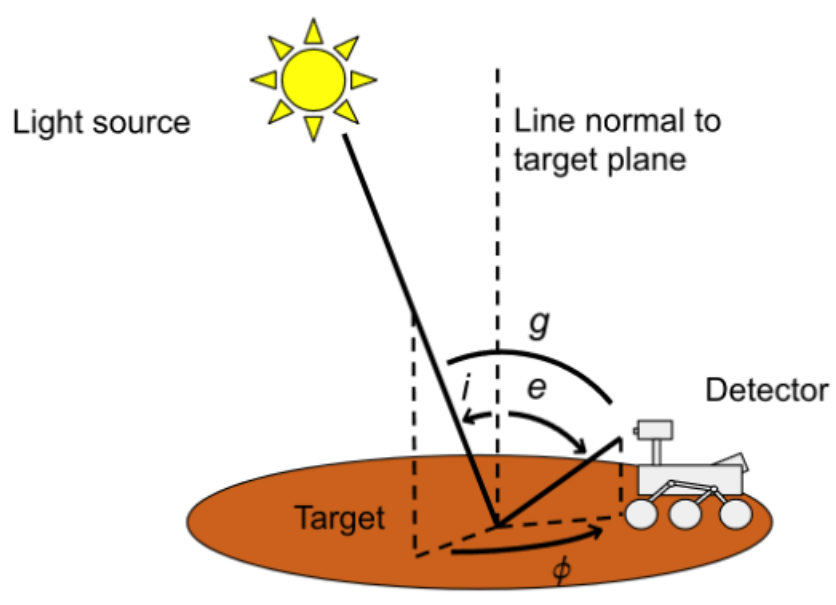
23

## 24 **1. Introduction**

25           Studying the composition and distribution of minerals on planetary bodies is critical to  
26 understanding their surface evolution. Across the solar system, key mineral identifications have  
27 been made using visible to near-infrared (VNIR) spectrometers on ground- and space-based  
28 telescopes, orbital spacecraft, and landers. VNIR reflectance spectroscopy relies on the analysis  
29 of diagnostic absorption features, specifically their band center wavelength positions, shapes, and  
30 depths (e.g., Bishop et al., 2020). However, VNIR reflectance spectra are not influenced by  
31 mineral composition alone. Variables such as grain morphology (size and shape), temperature,  
32 and nonlinear mixing effects also influence the shapes, positions and depths of diagnostic  
33 absorption features (e.g., Clark & Roush, 1984; Clark et al., 1999).

34           In particular, viewing geometry (photometric) effects can complicate remote sensing  
35 interpretations. Conversely, once understood, photometric effects can allow for richer inferences  
36 to be drawn than would otherwise be possible. For example, photometry has been used to  
37 constrain the microtexture of surface materials including roughness and porosity (e.g., Bandfield  
38 et al., 2015; Hapke and Sato, 2016; Shepard et al., 2017). Microtextural characteristics can in  
39 turn be used to understand surface processes (e.g., regolith/soil formation and evolution), to  
40 serve as inputs to planetary thermal models, and to constrain mechanical properties relevant to  
41 exploration. Such investigations have been performed for the Moon (e.g., Shkuratov et al., 1999),  
42 asteroids (e.g., Clark et al., 2002), Mars (e.g., Johnson et al., 1999; see also Fernando et al.,  
43 2015; Johnson et al., 2006a-b; Johnson et al., 2021, 2022; Lichtenberg et al., 2007) and other  
44 planets (e.g., Veverka et al., 1988; Schröder & Keller, 2009). Furthermore, several models have  
45 been developed to better understand how the microscale physical properties of surfaces influence  
46 photometry (e.g., Hapke, 1993; Shkuratov et al., 1999).

47 Photometric effects, however, are often not included in laboratory VNIR reflectance  
48 measurements of reference rocks and minerals. Many commercial VNIR spectrometers do not  
49 allow users to easily control the incidence and emission angles, and most laboratory spectra are  
50 acquired with a single, fixed geometry (e.g., incidence = 30°, emission = 0°). In contrast,  
51 telescopic and spacecraft observations of planetary surfaces are acquired at a variety of  
52 geometries, depending on the relative positions of the light source (Sun), target material  
53 (planetary surface), and detector (spectrometer/camera) (e.g., Figure 1). Custom-built  
54 goniometers (which control the orientations of the incidence light and spectrometer's detector)  
55 are required, therefore, for reproducing photometric effects in the laboratory.  
56



57  
58 **Figure 1.** Cartoon of viewing geometries relevant to spacecraft exploration of planetary  
59 surfaces, for the specific example of spectroscopy measurements by a rover on Mars. Geometries  
60 shown include emission angle  $e$ , incidence angle  $i$ , and azimuth angle  $\phi$ . Phase angle  $g$  is the  
61 angle between  $e$  and  $i$ .  
62

63 To date, such “spectrogoniometry” measurements have focused primarily on particulate  
64 samples of uniform grain size and composition (e.g., Pommerol et al., 2013; Shephard and

65 Helfenstein, 2007) or two-phase mixtures (e.g., Pilorget et al., 2016; Stack & Milliken, 2015). A  
66 limited number of laboratory studies have acquired spectrogoniometric measurements for whole  
67 rocks (Guinness et al., 1997; Shepherd & Arvidson, 1999). However, the compounding effects of  
68 composition, alteration, microtexture, and viewing geometry on complex rock surfaces are still  
69 poorly understood. Working with natural rock surfaces in the laboratory poses several  
70 challenges. For example, bulky samples require a non-standard goniometer setup with an  
71 adjustable sample stage and large incidence and emission arms.

72         We have designed and built such a system for the Mars Lab at Western Washington  
73 University (WWU) in order to characterize the spectrogoniometry of a variety of rock and  
74 mineral samples. Specifically, WWU's Mars Lab studies VNIR reflectance spectra of naturally-  
75 weathered rocks as analogs to the geologic materials encountered by the Mars Exploration  
76 Rovers (MERs), the Mars Science Laboratory (MSL) Curiosity rover, the Mars-2020  
77 Perseverance rover, and future landed missions. The science needs of the Mars Lab necessitate  
78 rapid acquisition of spectra from large numbers of bulky samples. For efficiency in collecting  
79 large datasets at high angular resolution, it is important to use a motorized system for precise,  
80 repeatable positioning of the light source, detector, and sample. Furthermore, software is  
81 required to automate the goniometer and allow it to interface with the spectrometer collecting the  
82 data. While some aspects of this ideal system have been developed previously for other  
83 laboratories (e.g., Biliouris et al., 2007; Camon & Lemelin, 2024; Painter et al., 2003; Pilorget et  
84 al., 2016; Pontin et al., 2018; Shepard and Helfenstein, 2007), no fully-automated system (to our  
85 knowledge) exists for goniometry with a hyperspectral instrument for measuring a variety of  
86 whole rock samples.

87           Here, we describe WWU’s Three-Axis N-sample Automated Goniometer for Evaluating  
88 Reflectance (TANAGER). (The acronym TANAGER also has local significance, as the Western  
89 Tanager is a brightly colored bird native to Washington state.) TANAGER derives heritage from  
90 the WWU Mars Lab’s previous planar goniometer (Hoza & Rice, 2019), which allows for  
91 automated collection of spectra from multiple bulky samples at varying incidence and emission  
92 angles. TANAGER substantially improves upon the planar goniometer design with the capability  
93 to collect out-of-plane geometries (i.e., varying azimuth), which is necessary to characterize the  
94 full bidirectional reflectance distribution function (BRDF). In partnership with the Seattle-based  
95 engineering company First Mode, LLC, we designed and characterized TANAGER to support  
96 rapid and comprehensive spectrogoniometric studies of natural rock samples.

97

## 98 **2. Performance Requirements**

99           To enable rapid collection of reflectance spectra from multiple rock surface across the  
100 full scattering hemisphere – as well as rapid analysis of the spectrophotometric datasets – we  
101 defined the following top-level requirements for TANAGER:

102           1.       **Scientific Purpose:** The system shall enable collection of VNIR spectra at  
103 a range of geometries relevant to spacecraft measurements.

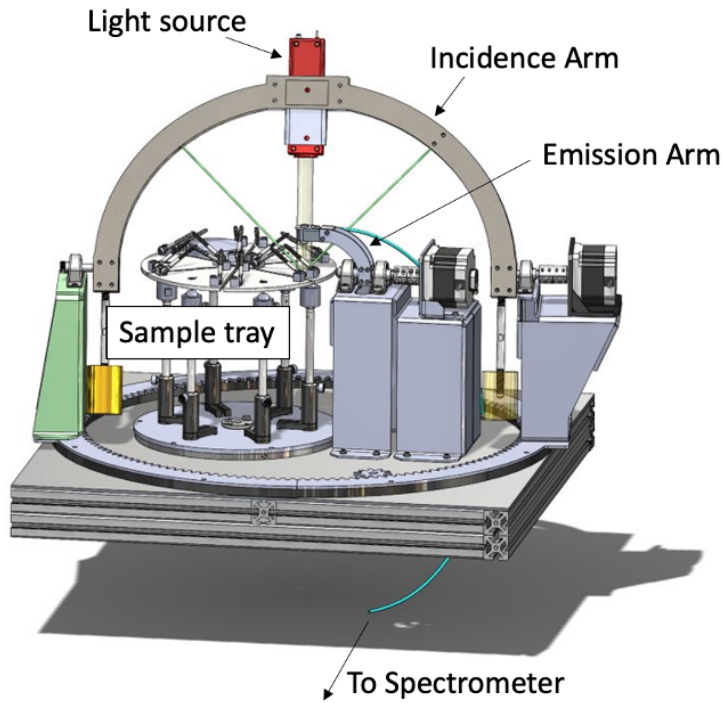
104           2.       **Sample Type:** The system shall enable measurement of bidirectional  
105 reflectance for natural, unprocessed samples.

106           3.       **Time Efficiency:** The system shall enable the following 2 concepts of  
107 operations: “Quick Runs” (8 hour time limit), and “Detailed Runs” (168 hour time limit).

108           4.       **Data Visualization:** The system shall provide a means of documenting  
109 and visualizing the collected spectra.

110                   5.       **Safety:** Use of the system shall not result in damage to people, the  
111                   goniometer, or other equipment, facilities, or samples.  
112 To meet these requirements, TANAGER’s high-level design (Figures 2-3) differs substantially  
113 from other spectrogoniometer systems, as we outline in Section 3.

114



115

116 **Figure 2.** Schematic of TANAGER with major components labeled. For scale, the dimensions of  
117 the baseplate are 80 x 95 cm.

118  
119



120



121 **Figure 3.** (left) TANAGER's final assembly at First Mode, LLC (photo by Kathleen Hoza);  
 122 (right) Samples being positioned on TANAGER's rotating sample tray for analyses in WWU's  
 123 Mars Lab (photo by Rhys Logan).  
 124

125 Each top-level requirement yields multiple sub-requirements (Table 1). First Mode, LLC  
 126 evaluated all requirements except for sub-requirements 1.13, 2.1, 2.2 and 2.4, which were  
 127 evaluated at WWU upon delivery of TANAGER in Spring 2021 (see Text S1-S5). Every sub-  
 128 requirement has been met except for the detector head not falling inside the incident light beam  
 129 for  $g \geq 20^\circ$  (sub-requirement 1.1). However, we find the small shadow cast at  $g = 20^\circ$  to be  
 130 acceptable, as it is outside the detector pointing (Figure S1). Eight of the sub-requirements were  
 131 also reevaluated after 300 hours of TANAGER run time (Table S1), which yielded  
 132 recommendations for long-term operations of the hardware (Table S6).

133

134 **Table 1:** Summary of the sub-requirements for TANAGER, which derive from the top-level requirements  
 135 listed in the text. All sub-requirements have been met except for 1.10 (which was met within an acceptable  
 136 threshold, as discussed in the text).

Sub-Requirement	Description
1.1 Range	The system shall enable measurements with <ul style="list-style-type: none"> <li>• azimuth from <math>0^\circ</math> to <math>170^\circ</math></li> <li>• emission from <math>-70^\circ</math> to <math>70^\circ</math></li> <li>• incidence from <math>-70^\circ</math> to <math>70^\circ</math></li> </ul>
1.2 Phase angle	The system shall enable measurements at phase angles from $10^\circ$ to $140^\circ$
1.3 Angular control	The system shall have knowledge and control of detector and light source with $1^\circ$ steps in all directions
1.5 Pointing accuracy - light source	The center of the illuminated spot shall not deviate from the target point by more than $\pm 10\%$ of the illuminated spot diameter
1.6 Pointing accuracy - detector	The center of the detector spot shall not deviate from the target point by more than $\pm 10\%$ of the detector spot diameter
1.7 Light bulb operating lifetime	The light bulb shall have an operating lifetime of at least 100 hours
1.8 Target plane indicator	The goniometer shall provide the user with a clear indicator of whether a surface is in the target plane

1.9 Proximity to light source	The detector head and fiber optic shall not come within 5 mm of the light source during normal operations
1.10 No incident light on detector	The detector head shall not be inside the incident light beam for $g \geq 20^\circ$
1.11 Signal drift from heating at small phase angles	At geometries with phase angles below $20^\circ$ , the standard deviation for repeated measurements taken over the course of 4 minutes shall not be greater than 0.02
1.12 Noise	For both light and dark samples, noise measured against a Savitzky-Golay smoothed spectrum with window size = 19, order = 2 shall not exceed <ul style="list-style-type: none"> <li>• +/- .001 in mid-range (500-2400 nm) wavelengths</li> <li>• +/- .005 for long (2400-2500 nm) and short (450-500 nm) wavelengths</li> </ul>
1.13 Polarization artifacts	Polarization artifacts shall not be more than 0.1 for basalt (or a similar sample) at any geometry where azimuth = $180^\circ$ or $0^\circ$
2.1 Detector spot size	The detector spot size on the sample shall have a diameter less than the size of the Spectralon puck at $e = 70^\circ$ (9.1 cm)
2.2 Light spot size	The brightest part of the light spot size shall be 0.5 cm to 3 cm in diameter at $i = 0^\circ$
2.3 Sample tray repeatability	Each of the 6 sample tray positions shall be repeatable to within +/- 1 mm
2.4 Sample tray vibration	Sample tray movements and vibrations from other actuators shall not disturb the positioning of rounded coarse sand grains in sample cups
2.5 Sample accommodation	The sample tray shall accommodate up to 5 cylindrical samples (9.1 cm diameter, 0 to 5.1 cm height) plus 1 Spectralon puck
2.6 Center-of-sample markings	The sample tray shall have marked center of sample points for each position
2.7 Large sample compatibility	The sample tray shall not interfere with the measurement of spectra for large (>10 cm) samples
2.8 Irregular sample positioning	The sample tray shall enable 5 different wedge-shaped samples plus the Spectralon puck to be positioned each with a surface that is: <ul style="list-style-type: none"> <li>• In the target plane to within +/- 1 mm</li> <li>• Parallel with the target plane to within +/- <math>5^\circ</math></li> <li>• Sample heights may range from 0-5 cm, diameters from 3-9 cm</li> </ul>
3.1 Viewing Geometries	Actuators shall be capable of positioning incidence, emission, and azimuth as described in sub-requirement 1.1
3.2 Sample tray rotation speed	Sample tray movements shall occur at an average speed of at least $4^\circ$ per second
3.3 Viewing geometry adjustment speed	Incidence, emission, and azimuth movements shall occur at an average speed of at least $0.2^\circ$ per second

3.4 Automatic software startup	Software on the spectrometer computer and raspberry pi shall start automatically
3.5 Legacy software	Unless otherwise noted, software shall provide the same functionalities and experience as existing software
3.6 Iteration across a range	Software shall enable data collection while iterating at a set interval through a range of incidence, emission, and azimuth angles as described in sub-requirement 1.1
3.7 Goniometer visualization	Software shall provide a visualization showing the software's understanding of the current state of the 3D goniometer including incidence angle, emission angle, azimuth angle, and sample tray position
3.8 Communication speed (microcontroller)	Communicating commands to and from the microcontroller shall take no longer than 1 second
3.9 Communication speed (spectrometer computer)	Communicating commands to and from the spectrometer computer shall take no longer than 1 second
3.10 Time limit (limited run)	A limited run of data collection shall take no longer than 8 hours
3.11 Number of samples (limited run)	A limited run of data collection shall characterize 1 sample
3.12 Viewing geometries (limited run)	A limited run of data collection shall include the following geometries: <ul style="list-style-type: none"> <li>• For a single plane (<math>az = 0^\circ</math>) measure <math>e, i</math> with <math>10^\circ</math> resolution</li> <li>• Outside that plane - <math>30^\circ</math> azimuthal resolution, 5 geometries at each azimuth</li> <li>• Leave out reciprocal and rotationally equivalent geometries</li> </ul>
3.13 Time limit (detailed run)	A detailed run of data collection shall take no longer than 168 hours
3.14 Number of samples (detailed run)	A detailed run of data collection shall characterize 5 samples
3.15 Viewing geometries (detailed run)	A detailed run of data collection shall include the following geometries: <ul style="list-style-type: none"> <li>• <math>30^\circ</math> azimuthal resolution</li> <li>• At each azimuth, <math>10^\circ</math> angular resolution for incidence, emission</li> </ul>
3.16 Spectra per sample	At each geometry, a measurement of a single sample shall consist of averaging 200 spectra
3.17 Human operator time	Setting up a run of data collection shall not require more than 60 minutes of time from a human operator
4.1 Data processing/ visualization	Software shall be capable of processing and plotting data sets of up to 5000 spectra
4.2 Feature requests	Additional features may be added
5.1 Light source casing temperature	The temperature of the light source shall not exceed $60^\circ$ C

5.2 Securability	The sample tray shall be securable
5.3 Position detection	The goniometer incidence, azimuth, and emission positions and the sample tray position shall be detected at the start of operations
5.4 Collision avoidance	Software shall not allow incidence, emission, or azimuth arms to collide with each other

137

138

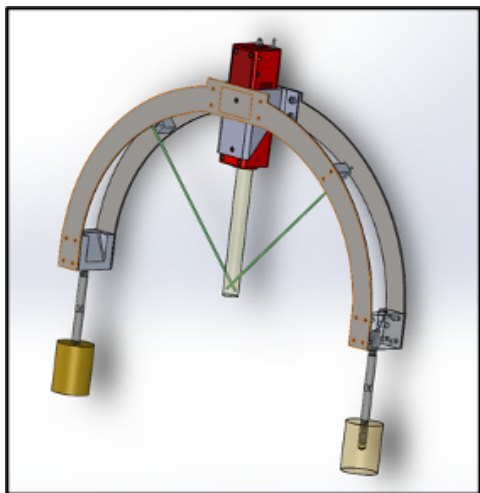
### 139 **3. Design and Characterization**

#### 140 *3.1 Incidence Arm and Light Source*

141           The primary design difference between TANAGER and most existing goniometers is the  
142 use of rotating and tilting arcs instead of straight arms, with the addition of cylindrical bronze  
143 ~1.5 kg counterbalance weights to provide stability and require less torque from the motors  
144 (Figure 4). The TANAGER system enables incidence and emission angles of  $-70^\circ$  to  $70^\circ$ , and  
145 stepper motors allow for automated, repeatable movements to defined geometries sampling the  
146 full scattering hemisphere. This range of angles is sufficient to characterize scattering behavior  
147 using the Hapke model (e.g., Schmidt and Fernando, 2015).

148           Using two green laser guides on the incidence arm (Figure 5), we can ensure that the  
149 surfaces of bulky samples are positioned precisely in the focal plane. The brightest portion of the  
150 illuminated spot size in the focal plane at  $i = 0^\circ$  is 2.7 cm in diameter, and larger at higher  
151 incidence angles (but always  $<9.1$  cm, per sub-requirement 2.2; Table 1). Because the  
152 illuminated spot size is not actively controlled, it is possible to measure slightly different  
153 portions of the sample surface at different incidence angles, especially with high emission angles  
154 where the detector spot (which is similarly not actively controlled) can be larger than the

155 illuminated spot. Users should take this into consideration for high phase angle measurements of  
156 non-uniform samples.



157  
158 **Figure 4.** Schematic of TANAGER's incidence arm. The diameter of the arc is 67 cm.  
159 Illumination is provided by a Thorlabs VNIR light source, and two bronze weights provide  
160 counterbalance. Two green laser guides intersect at the focal plane.  
161



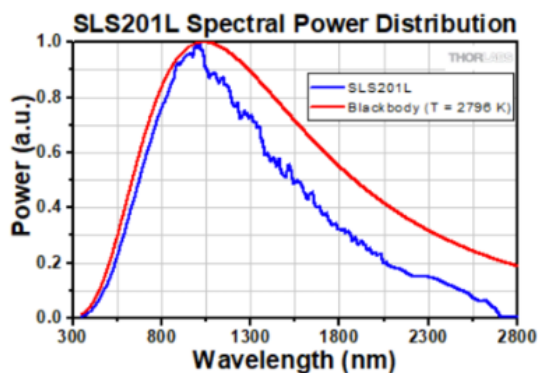
162  
163 **Figure 5.** Green laser guides indicate when the sample is out of the focal plane (left) and within  
164 the focal plane (right, when two dots become one).  
165

166 The apex of the incidence arm supports a Thorlabs SLS201L light source with integrated  
167 cooling system and peak output near 1000 nm (Figure 6). This commercial light was selected for  
168 its relatively long bulb lifetime, sufficient power output across the 400-2500 nm wavelength  
169 range, and minimal heating. We characterized heating on color standards and geologic targets in  
170 the focal plane (Text S1) and found the temperature increases to be minimal: Spectralon®, which

171 heated negligibly (0.4°C), and other targets' temperatures increased by 2-4°C over typical  
172 exposure durations (~2 minutes of direct illumination during nominal TANAGER operations)  
173 (Figure S2). We also characterized the effects of incident light heating on adsorbed water by  
174 monitoring spectral changes to powdered anhydrite (CaSO<sub>4</sub>) over time (Text S2). During 30  
175 minute periods of exposure, we observed no changes to the hydration absorptions attributed to  
176 adsorbed water on grain surfaces (Figures S2-S4), which gives us confidence that the sample  
177 heating is too minimal to drive adsorbed water off mineral grains or otherwise dehydrate  
178 samples.

179

Optical power: 500 mW



180

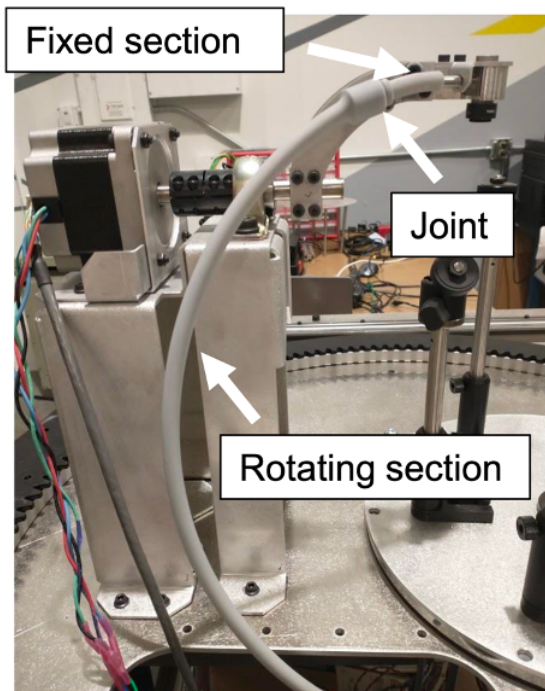
181 **Figure 6.** Thorlabs VNIR light source (left) with power distribution curve for a blackbody and as  
182 measured (right).

183

### 184 3.2 Emission Arm

185 TANAGER interfaces with a Malvern PanAnalytical ASD FieldSpec4 Hi-Res reflectance  
186 spectrometer (hereafter, "FieldSpec"; Section 3.5), and its emission arm is designed to  
187 accommodate the fiber optic cable attached to the spectrometer (the reflectance probe). Like the  
188 incidence arm, the emission arm uses stepper motors for precise, repeatable positioning of  
189 emission angles from -70° to 70°. The design of the arm is an arc (Figure 7) with a collimating

190 lens that reduces the detector spot size at the focal point. Reflected light entering the collimator  
 191 is directed to the fiber optic cable via an angled mirror at the end of the emission arm. We  
 192 characterized how the detector spot size changes with emission angle (Text S3) and found a  
 193 minimum of 1.6 cm at  $e = 0^\circ$  and a maximum of 3.5 cm at  $e = 70^\circ$  (Table 2). At small incidence  
 194 angles, this means that the detector spot falls entirely within the illuminated portion of the  
 195 sample for emission angles  $< 50^\circ$ .



196  
 197  
 198 **Figure 7:** Components of the emission arm's tubing, which guides the position of the FieldSpec's  
 199 fiber optic cable and maintains a wide arc at all geometries.  
 200

201 **Table 2:** Detector spot size ranges measured for different emission angles (see Text S1).

Emission angle ( $^\circ$ )	Measured Spot Size Range (cm)
0	1.6-2.0
15	1.8-2.6
30	1.8-2.2
50	2.4-2.8
70	2.8-3.5

202

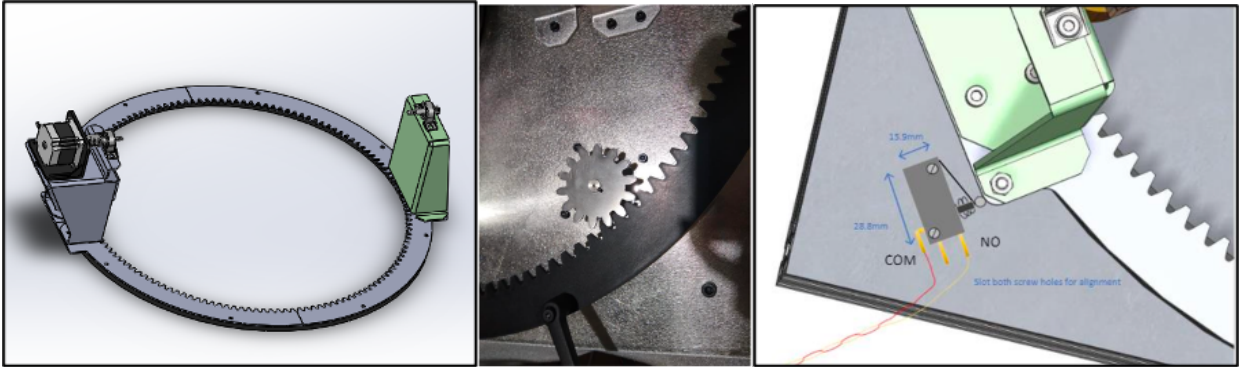
203           The emission arm design ensures that the spectrometer’s fiber optic cable (the reflectance  
204 probe) does not bend in any geometry. A guide tube keeps the fiber in a repeatable position from  
205 one measurement to the next, which consists of a short, fixed portion close to the detector tip and  
206 a longer, rotating portion farther back (Figure 7). This tubing allows for the fiber optic to be  
207 easily removed and replaced when the FieldSpec needs to be detached from TANAGER (e.g.,  
208 when used with a Malvern Panalytical Contact Probe or Small Diameter Probe). To prevent  
209 bending of the fiber optic, the system is designed to maintain a 35 cm diameter of curvature.

210

### 211 *3.3 Azimuth Turntable*

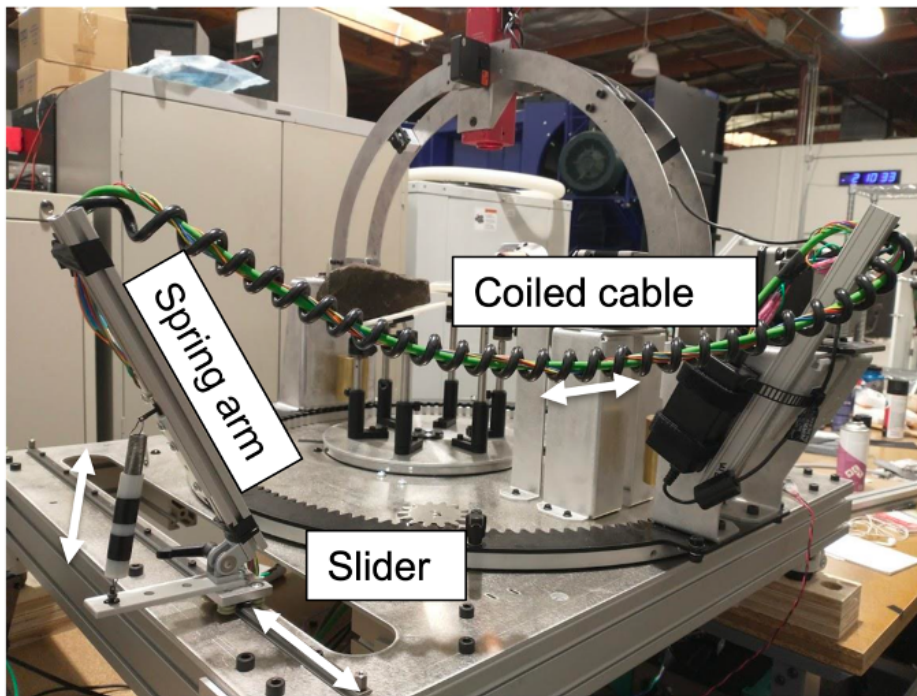
212           The incidence arm is mounted to a geared turntable which controls azimuth angle  
213 between 0° and 180° (Figure 8). The large gear ratio reduces the necessary torque and increases  
214 angular accuracy. The system includes a homing routine with stops installed onto the baseplate.  
215 One challenge in the azimuth design is the need to manage cables for the light source, incidence  
216 motor, and incidence encoder as azimuth changes. The solution in TANAGER’s initial design  
217 used the combination of slider, coiled cable, and spring-loaded arm to enable consistent motion  
218 across the azimuth range (Figure 9). However, upon extensive use in WWU’s Mars Lab, we  
219 found that the slider’s and spring arm’s motions were finicky, so we attached the coiled cable to  
220 a fixed lab surface with ample clearance instead (Figure 10).

221



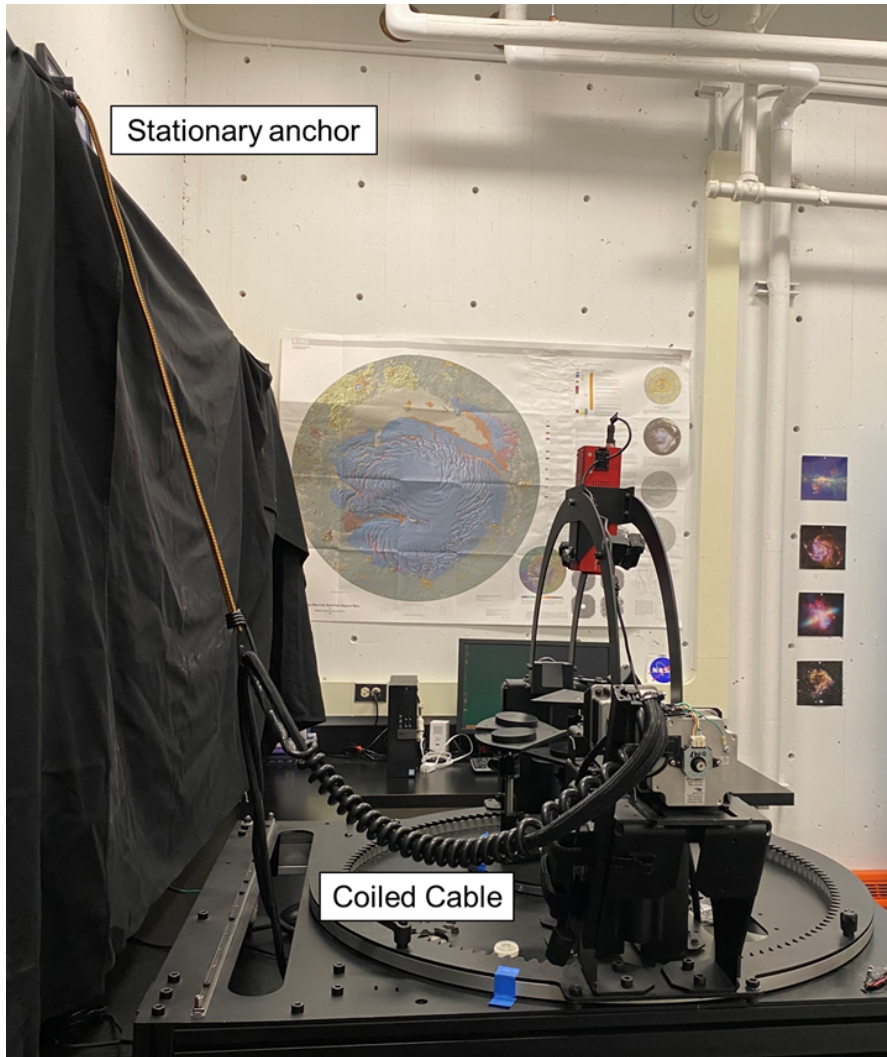
222  
 223  
 224  
 225  
 226  
 227

**Figure 8.** Left: Schematic of the azimuth turntable mounted with the attachments and stepper motor for the incidence arm. Middle: Detail of gears for the azimuth turntable. Right: Schematic of the homing mechanism on the azimuth baseplate.



228  
 229  
 230

**Figure 9.** Initial cable management solution for the full range of azimuths ( $0^\circ$  to  $180^\circ$ ).



231

232 **Figure 10.** Final cable management solution for the full range of azimuths ( $0^{\circ}$  to  $180^{\circ}$ ).

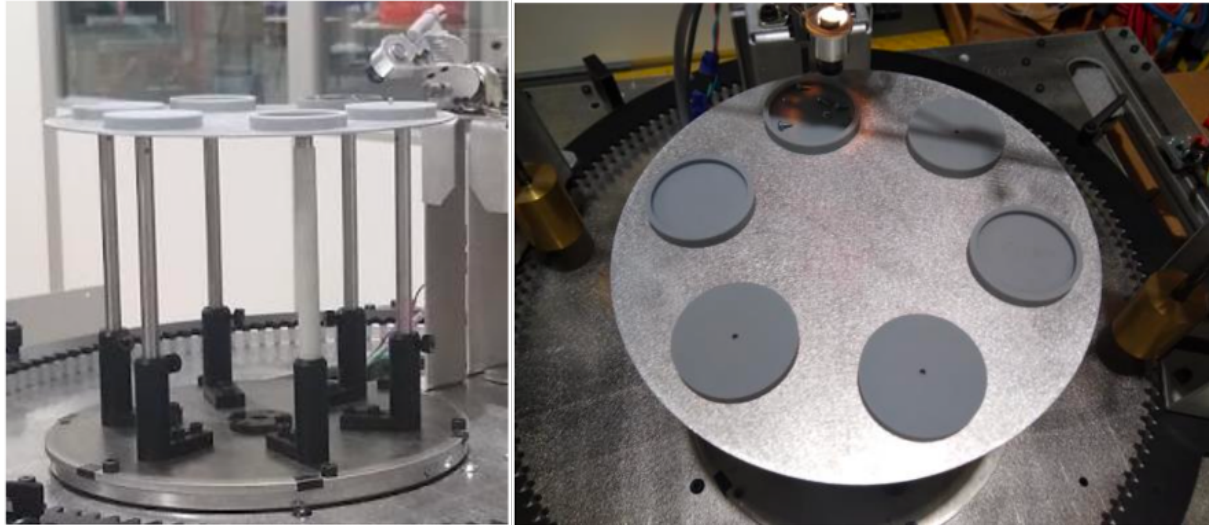
233

### 234 3.3 Sample Trays

235 The goniometer design includes two stages for positioning samples within the focal  
236 plane. Both are motorized and can rotate up to five samples in and out of the field of view with a  
237 Spectralon<sup>®</sup> white reference correction at each geometry. The first is a single, height-adjustable  
238 surface designed for multiple samples of the same height (e.g., particulates in sample cups) or for  
239 a single, bulky hand sample (Figure 11). For use with this stage, we designed sample cups at the

240 same height as the white reference and risers for positioning Scanning Electron Microscope  
241 (SEM) mounted samples.

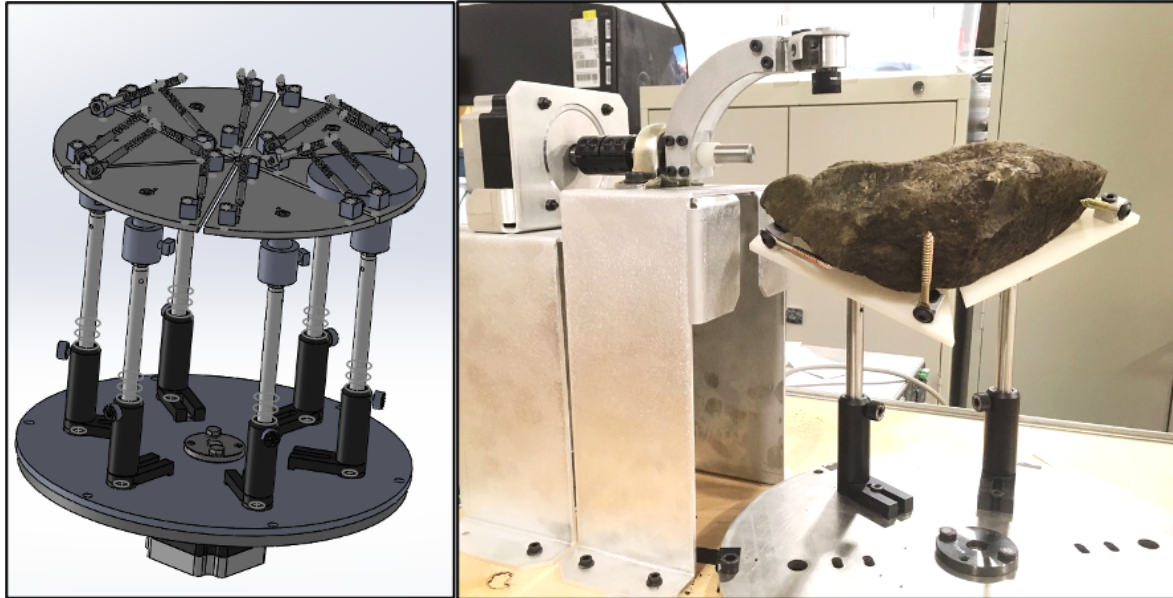
242



243

244 **Figure 11.** *Left: Single-height, rotating sample stage. Right: Custom sample cups and risers for*  
245 *SEM mounts designed with the same height as the Spectralon<sup>®</sup> white reference puck.*  
246

247 The other stage consists of six pie-slice-shaped sample supports, each of which can be  
248 moved independently (height and tilt) to accommodate a variety of bulky samples (Figure 12).  
249 Many degrees of freedom are required for positioning a near-flat portion of each sample into the  
250 focal plane. Adjustable screws can be added/removed to keep samples in place, and multiple  
251 sample supports can be used to support a single, awkward sample (Figure 12 right). In  
252 characterizations of sample tray motion during TANAGER operations (Text S4), we found that  
253 vibration was undetectable during incidence and emission arm motions, and minimal during  
254 azimuth and tray motions (Figure S5). TANAGER's movements are highly unlikely to change  
255 the positions of samples on the tray or shift loose material within sample cups (Figure S6).  
256



257

258 **Figure 12.** Left: Schematic of the multi-height, rotating sample stage. Six independently-  
259 adjustable, pie-slice-shaped supports allow for the positioning of a variety of samples. Right:  
260 Example of a bulky, awkward sample positioned with a horizontal surface in the focal plane  
261 using two supports and stabilizer screws.

262

### 263 3.4 Paint

264 Before delivery of TANAGER, all components were coated with a matte black paint to  
265 minimize stray light reflections from the metallic surfaces. We collected VNIR spectra for a  
266 range of different black paint options (LabIR Paints, Rustoleum, Fusion, black30), and all  
267 exhibited similar spectral shapes and low albedos throughout the 400-2500 nm range. Specular  
268 properties for all materials were also similar. Thus, we looked to mechanical adhesion and wear  
269 and selected LabIR Paints (<https://paints.labir.cz/en/>) because it performed best in mechanical  
270 tests. We applied the black paint to TANAGER via aerosol (Figure 3).

271

### 272 3.5 Spectrometer Interface

273 Sample spectra (averages of 200 for each) are measured relative to a Spectralon® white  
274 reference target at each geometry and corrected for minor (<2%) irregularities in absolute  
275 reflectance and for small offsets at 1000 and 1830 nm where detector changeovers occur (e.g.,  
276 Cloutis et al., 2008). The ideal white reference material would be a perfectly Lambertian  
277 reflector (scattering incident light equally at all viewing geometries); in practice, however, such a  
278 material does not exist, but the geometry-dependent reflectance properties of Spectralon® have  
279 been well-documented (e.g., Shaw et al., 2016). We have incorporated the published Spectralon®  
280 corrections for high phase angles from Bhandari et al. (2012), using a linear interpolation when  
281 needed, into the analysis software (Section 2.9).

282 Other challenges to the spectrometer interface occur at high phase angles, where the  
283 emergence of artifacts near 1100 and 1310 nm in spectra from FieldSpec and similar  
284 spectrometers have been documented (e.g., Buz et al., 2019) and shown to originate from  
285 polarization of the sample and probe (Levesque & Dissanska, 2016). These polarization artifacts  
286 are challenging to correct, but fortunately, their wavelength positions do not interfere with the  
287 locations of the prominent spectral features and absorptions in rock-forming minerals and their  
288 alteration products. We quantified the strength of these artifacts for our prototype planar  
289 goniometer (Hoza & Rice, 2019), for a variety of materials at a range of phase angles, and found  
290 that they were consistently negligible (<1%) at phase angles between  $g = -20^\circ$  and  $g = 40^\circ$ .  
291 Therefore, we designed an option to omit the region 1050-1350 nm from TANAGER's high  
292 phase angle analyses, as done by Buz et al. (2019). However, we have rarely needed this option

293 in practice, as TANAGER’s spectra rarely exhibit polarization artifacts (and, when they do  
294 appear, they are < 2%; Text S5; Figure S7).

295

### 296 *3.6 Automation and Control Software*

297 Automation is a critical design component of TANAGER. Our previous studies verified  
298 the need for an automated system: using our prototype planar goniometer (Hoza & Rice, 2019)  
299 with a simple control software, we found that our rate of data collection increased by almost an  
300 order of magnitude. When manually positioning targets and the goniometer arms, acquiring  
301 measurements at 10 viewing geometries with Spectralon<sup>®</sup> white reference correction took  
302 roughly 90 minutes for a single sample and required an attendant in the lab to adjust the  
303 goniometer and perform the white reference calibration every few minutes. However, with  
304 automation, we acquired spectra of five samples with white reference corrections at 10 viewing  
305 geometries each in under 60 minutes total, including time for data processing and plotting, with  
306 minimal need for supervision by a lab attendant (Hoza & Rice, 2019). For more detailed analyses  
307 requiring high angular resolution (~100 geometries), automation reduced the total acquisition  
308 time per sample from ~15 to ~2 hours.

309 For TANAGER, a total of four stepper motors drive the incidence, emission, azimuth,  
310 and sample tray components, as described above. First Mode, LLC designed custom software for  
311 TANAGER in open source packages called “tanager-feeder” (Hoza, 2023). The software  
312 operates three computers all connected to a local spectroscopy lab network (Figure 13):

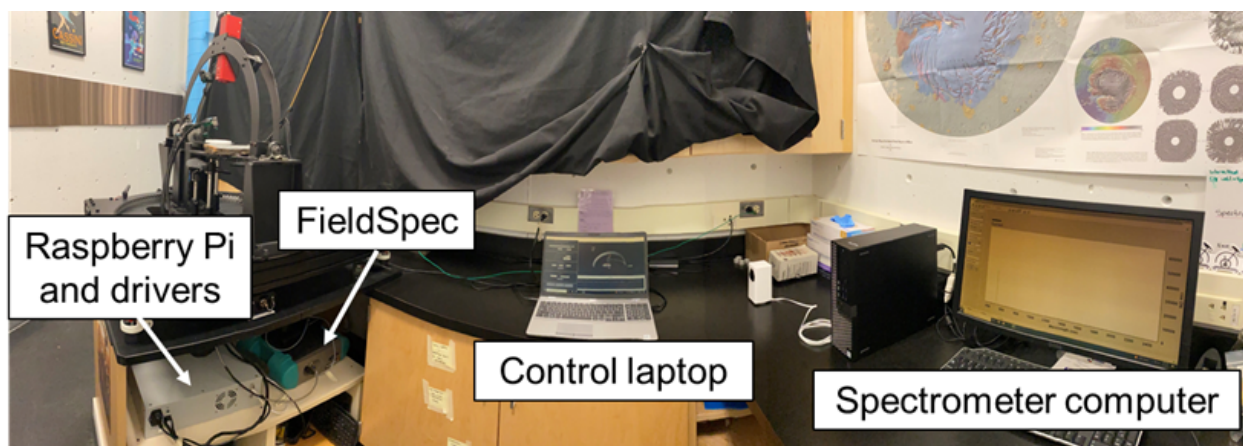
313 1. *Control computer.* This is where the user gives input. Software running on this  
314 computer includes a Python Graphical User Interface (GUI) that allows the user to input  
315 all parameters relating to sample configuration, spectrometer configuration, and desired

316 viewing geometries. This GUI also displays information about the current state of the  
317 system (Figure 14) and includes a log of all actions taken during the current session.

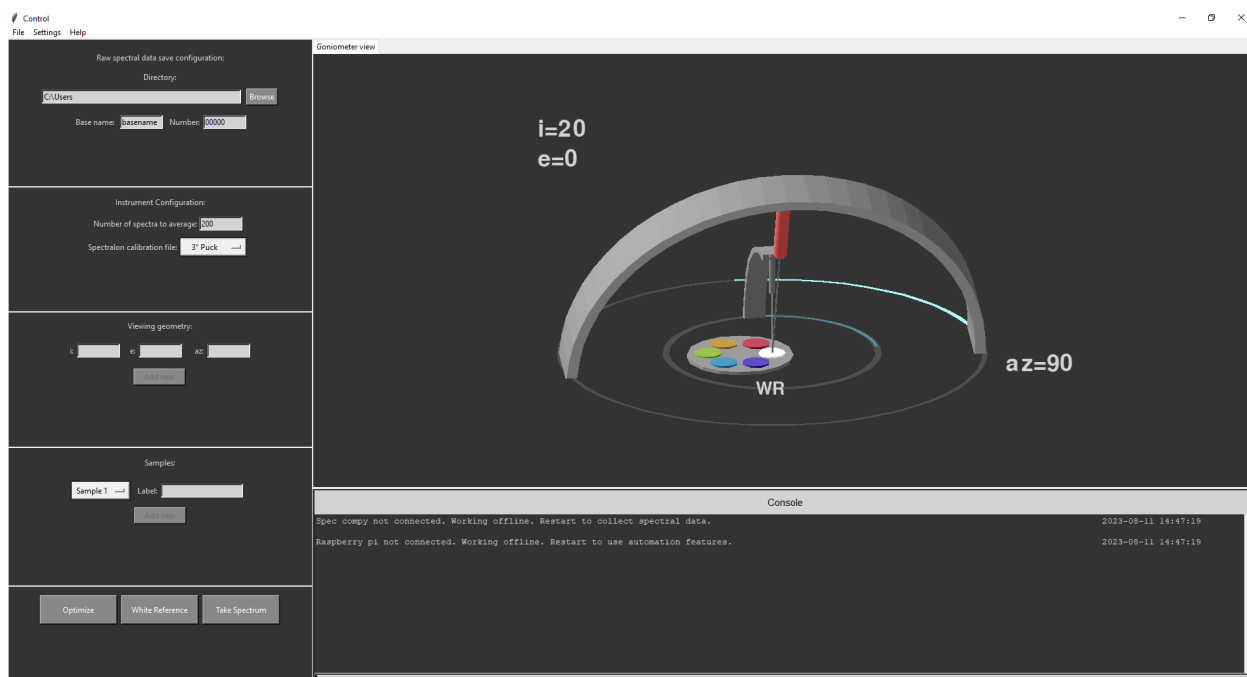
318 2. *Spectrometer computer*. This computer is controlled via command files generated by  
319 the control computer and dropped into a shared folder on the local network. Following  
320 instructions in these command files, it runs GUI automation software that operates the  
321 proprietary spectrometer control software (RS3) and spectral processing software  
322 (ViewSpec Pro). This enables the instrument to be optimized and for a white reference  
323 taken at each viewing geometry. After each run of data collection, this spectral  
324 processing software is used to apply a splice correction to remove artifacts generated at  
325 the positions where spectrometer detectors overlap.

326 3. *Raspberry Pi*. This computer is also controlled via command files generated by the  
327 control computer and dropped into a shared folder on the local network. Following  
328 instructions in these command files, it operates the motors driving the goniometer arms  
329 and sample tray. The software is designed with safety in mind; for example, it keeps the  
330 emission and incidence arms out of harm's way while other parts are rotating. The  
331 control system also notices if motorized parts are not making progress and stops and  
332 alerts the user via the control computer.

333



334  
 335 **Figure 13.** Panoramic photo of the lab containing TANAGER (upper left) showing the relative  
 336 placements of the FieldSpec, Raspberry Pi, control laptop, and spectrometer computer. Blackout  
 337 curtains are hung behind TANAGER in order to minimize stray light.  
 338

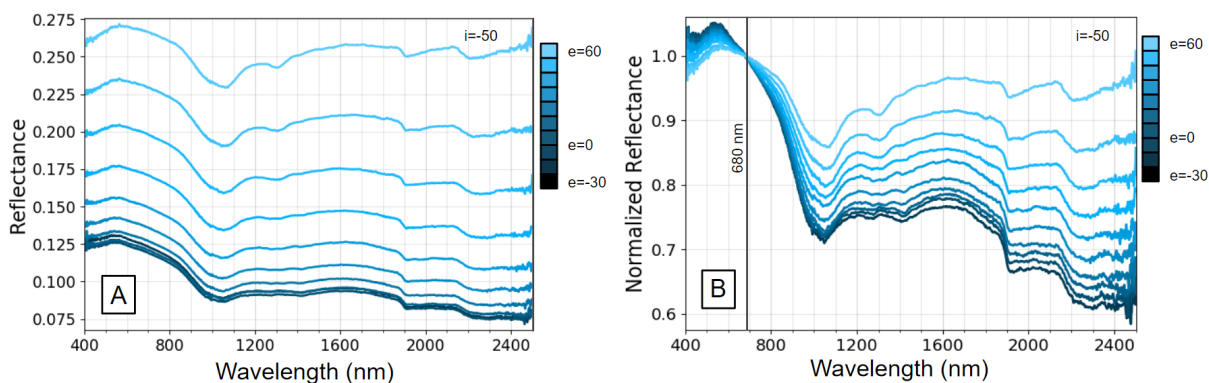


339  
 340 **Figure 14.** Screenshot of “tanager-feeder” control software GUI with settings on the left,  
 341 visualization of current goniometer and sample stage configuration on the upper right, and  
 342 command line interface at lower right.  
 343

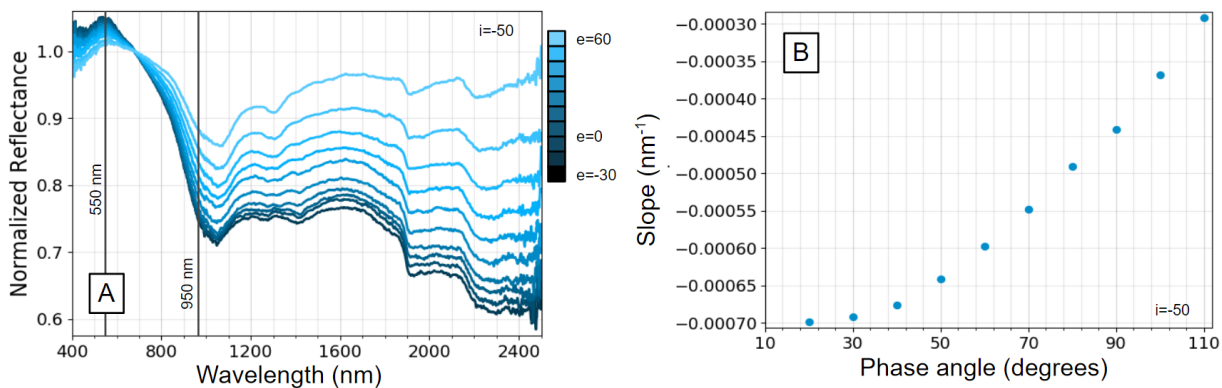
### 344 3.7 Analysis Software

345 In addition to operating the goniometer and spectrometer, the “tanager-feeder” software  
 346 includes a suite of tools that can be used to view and analyze spectrophotometric data. In the

347 simplest case, a selected set of spectra are plotted with wavelength on the x-axis in nanometers  
 348 and reflectance (relative or absolute) on the y-axis (Figure 15a). Additional analytical  
 349 capabilities include normalizing spectra to 1.0 at a given wavelength (Figure 15b); calculating  
 350 spectral slope (defined as the change in relative reflectance divided by the change in wavelength  
 351 in nm; Figure 16); calculating band centers and depths of features between user-defined shoulder  
 352 wavelength positions (as defined by Clark, 1999); calculating average reflectance for all values  
 353 between a give wavelength range; adding offset values to spectra for clarity (Figure 17); and  
 354 excluding wavelength regions with known artifacts (Figure 18).  
 355

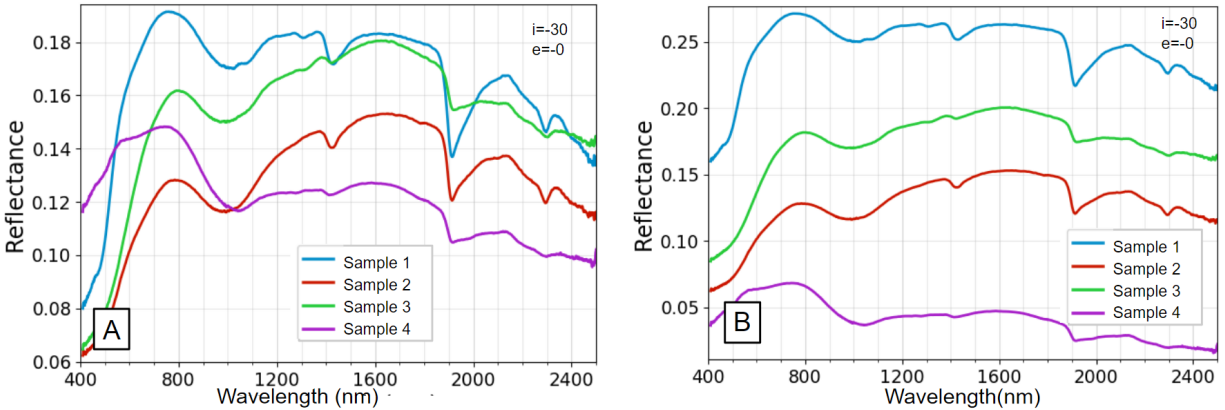


356  
 357 **Figure 15:** Example of spectra before (a) and after (b) normalization to 1.0 at wavelength 680  
 358 nm.

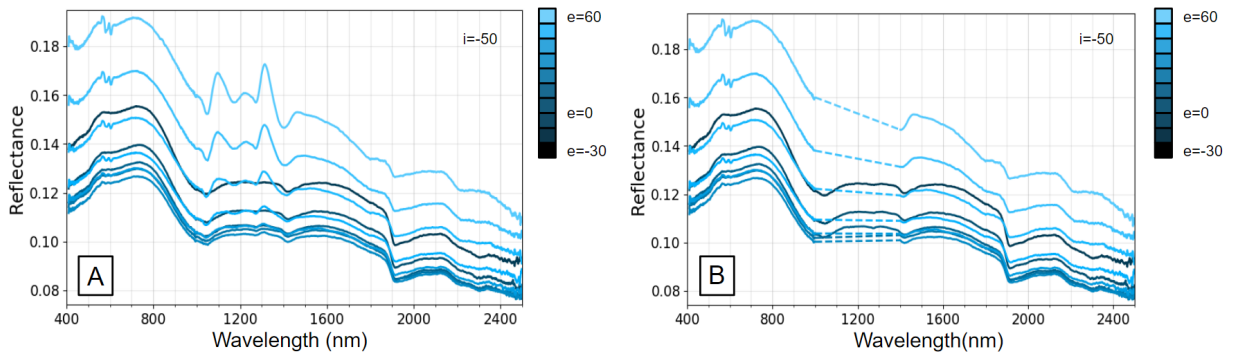


359

360 **Figure 16:** Spectral slopes are calculated from a range of wavelengths identified for spectra of  
 361 interest (a) and can be plotted as a function of phase angle  $g$  (b). In this case, slopes are  
 362 calculated from 550-950 nm and are shown to become less negative as phase angle increases.  
 363



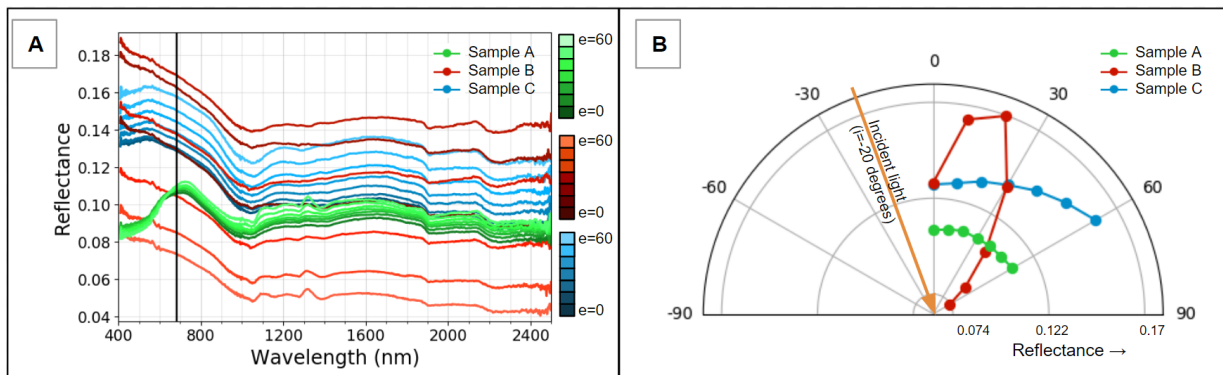
364  
 365 **Figure 17:** Overlapping spectra (a) can be hard to interpret, but adding offsets to samples can  
 366 add clarity (b).  
 367



368  
 369 **Figure 18:** Polarization artifacts can appear within wavelengths 1000-1400 nm at high phase  
 370 angles (a), so these regions can be omitted from our results for given geometries and replaced  
 371 with dashed lines (b). Spectra shown are from the WWU Mars Lab's planar goniometer (Hoza &  
 372 Rice, 2019); in practice, TANAGER spectra rarely exhibit polarization artifacts (Text S5; Figure  
 373 S7).  
 374  
 375

376 When interpreting spectra taken at a wide range of geometries, alternative visualization  
 377 techniques can be beneficial for displaying some photometric behaviors. For example, to show  
 378 the shapes of scattering lobes for measurements in a single plane (fixed azimuth), two-  
 379 dimensional hemispherical plots can be much more effective than the original spectra (Figure

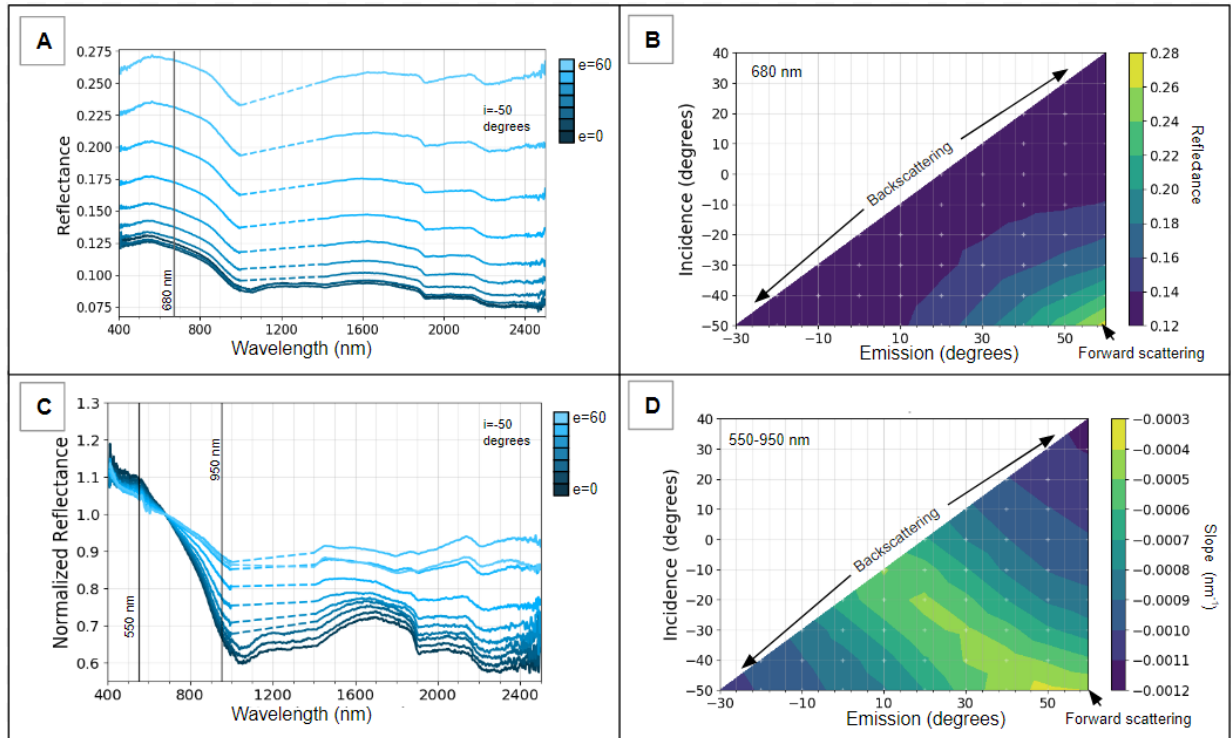
380 19). Our software also allows fixed azimuth data to be displayed with a heatmap; in these plots,  
381 emission angle is on the x-axis, incidence angle on the y-axis, and a user-defined parameter  
382 (such as reflectance at a given wavelength, band depth of a specific features, etc.) is represented  
383 by a color scale (Figure 20). For three-dimensional datasets (including variations in azimuth  
384 angle), the software enables visualizations of spectrophotometric behaviors as scattering lobes  
385 and/or heatmaps (Figure 21).  
386



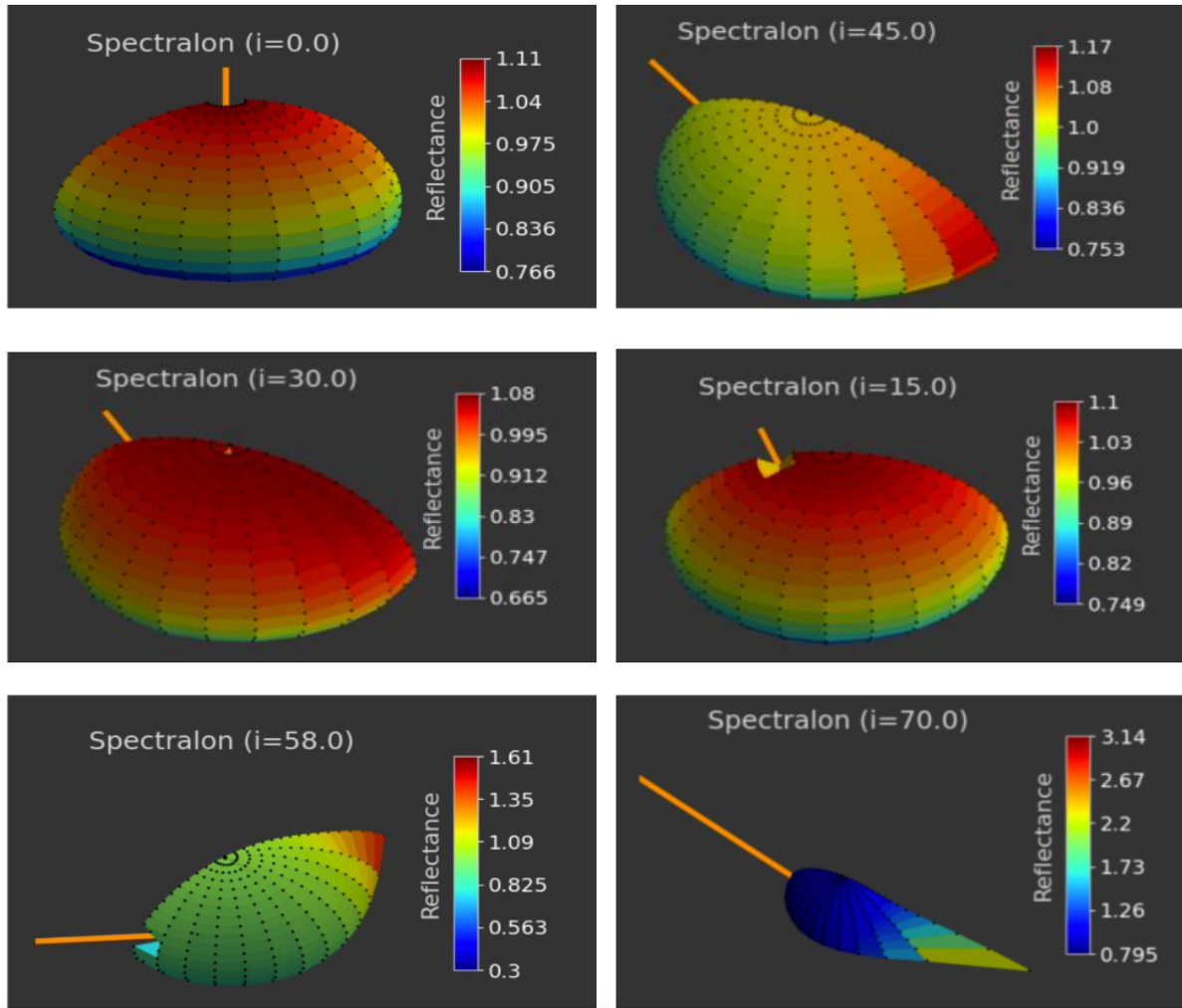
387  
388  
389  
390  
391  
392  
393  
394

**Figure 19:** Examples of two-dimensional hemispherical plots: (a) Reflectance is measured for three samples at an incidence angle of -20 degrees and emission angles varying from 0 degrees to 60 degrees. (b) Reflectance values at 680 nm are plotted on a hemispherical plot with reflectance on the radial axis and emission angle varying with theta. Spectra shown are of uncoated (blue, green) and silica-coated (red) basalt surfaces (Hoza, 2019).

395



396 **Figure 20:** Examples of two dimensional “heat map” plots: (a) Reflectance is measured at 6all  
397 viewing geometries for a given sample (incidence = -50° shown here). (b) Reflectance at 680 nm  
398 is plotted as a heat map in incidence, emission space with a color scale representing a range of  
399 reflectance. (c) For a different sample, slope from 550-950 nm is measured for normalized  
400 spectra at all viewing geometries (incidence = -50° displayed here). (d) Slope is then plotted on  
401 a heat map over incidence, emission space with the color scale corresponding to different slopes.  
402



403

404 **Figure 21:** Examples of three-dimensional hemispherical plots of scattering patterns for the  
 405 Spectralon® white reference (which is non-Lambertian above  $i= 45^\circ$ ), for reflectance values at  
 406 680 nm.  
 407

### 408 3.8 Operational Procedures

409         Approximately one hour of human operation time is required before TANAGER data  
 410 collection can be initiated. A number of startup procedures are required to place and secure  
 411 samples, perform safety checks, input run parameters, and generally ensure that data are  
 412 collected safely and effectively. Below, we provide a high-level description of human-operator  
 413 startup tasks for TANAGER data collection in “automatic mode”:

- 414 1. *FieldSpec warmup*: Turn on the FieldSpec spectrometer to allow it to warm up for  
415 60 minutes, as recommended by the manufacturer (ASD Inc., 2017).
- 416 2. *Sample positioning (initial)*: While the FieldSpec is warming up, perform the  
417 initial sample placements on the sample stage, level targets using a bubble level,  
418 and adjust the targets into the measurement plane with the indicator lasers (Figure  
419 5). For larger, natural, or irregular samples, this may require significant  
420 manipulation of the sample tray stage and/or securing the sample with supports  
421 and stabilizer screws (Figure 12). Finally, test for collisions by manually moving  
422 the emission arm to  $\pm 50^\circ$  (the steepest emission angle during sample tray  
423 rotation), rotating the sample tray  $360^\circ$ , and readjusting sample placement as  
424 necessary.
- 425 3. *Software setup*: After initial sample placement, turn on the Raspberry Pi, control  
426 computer, and spectrometer computer. In the user interface on the control laptop,  
427 configure the control computer interface to match the physical TANAGER set up,  
428 set the number of spectra to be collected, select the correct white reference  
429 calibration file, enter the desired geometries, and name the samples.
- 430 4. *Sample positioning (secondary)*: With Raspberry Pi on and the stepper motors  
431 engaged, recheck the sample placement, leveling, height, and collision risk for  
432 each sample and make final adjustments as necessary.
- 433 5. *Data collection*: During data collection, light sources unrelated to data collection  
434 (e.g. overhead lights and unnecessary computer monitors) should be turned off. A  
435 human operator may either remain in the lab (e.g. for a short run of 30 minutes) or  
436 leave the lab for the duration of the run (e.g. for multi-day runs) in order to

437 eliminate stray light from outside the lab. Western Mars Lab uses an infrared  
438 webcam to monitor the control computer software and TANAGER hardware for  
439 run completion or unexpected errors when the human operator is not in the lab.

440

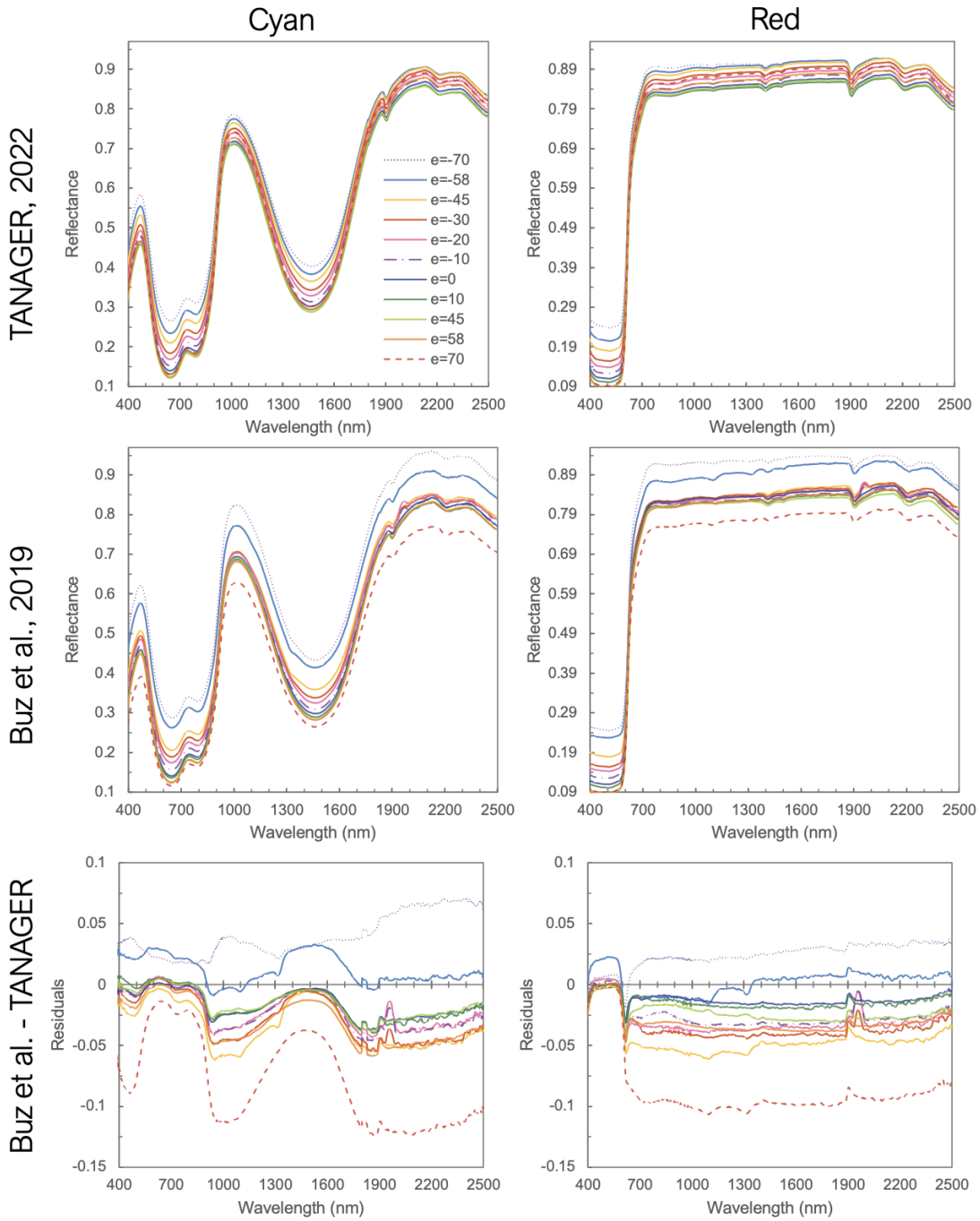
## 441 **4. Data Validation**

### 442 *4.1 Cross-Calibration*

443 We validated TANAGER’s data quality by reproducing measurements of calibration  
444 target (“caltarget”) materials from Buz et al. (2019). The caltargets are a set of exceptionally well  
445 characterized color standards and are the reference targets for the Mastcam-Z instrument on the  
446 NASA Mars 2020 *Perseverance* rover (Kinch et al., 2020). These caltargets have also been used  
447 in the calibration of Mastcam-Z’s legacy instruments: Mastcam on the NASA Mars Science  
448 Laboratory *Curiosity* rover (Bell et al., 2017) and Pancam on the NASA Mars Exploration  
449 Rovers (Bell et al., 2006). The eight caltargets include AluWhite from Avian Technologies LLC;  
450 and Cyan, Green, Red, Yellow, Gray33, Gray70, and Black from Lucidion Inc.. Spectra from  
451 each target were collected at same geometries of Buz et al. (2019) and evaluated at subset of  
452 phase angles: backscattering geometry ( $i = 30^\circ$ ,  $e = 45^\circ$ ,  $az = 0^\circ$ ,  $g = 15^\circ$ ), standard geometry ( $i =$   
453  $0^\circ$ ,  $e = 30^\circ$ ,  $az = 0^\circ$ ,  $g = 30^\circ$ ), specular geometry ( $i = -30^\circ$ ,  $e = 30^\circ$ ,  $az = 0^\circ$ ,  $g = 60^\circ$ ), forward  
454 scattering geometry ( $i = -45^\circ$ ,  $e = 30^\circ$ ,  $az = 0^\circ$ ,  $g = 75^\circ$ ), and very forward scattering geometry ( $i =$   
455  $-70^\circ$ ,  $e = 58^\circ$ ,  $az = 0^\circ$ ,  $g = 128^\circ$ ). Relative root mean square error (RMSE, defined in Text S3)  
456 was calculated to compare datasets. We consider a relative RMSE of 5% or less to be an  
457 acceptable threshold of error (as is the case in the radiometric calibration of flight hardware such  
458 as Mastcam-Z; Hayes et al., 2021).

459 Spectra from TANAGER agree with those from Buz et al. (2019) to within 0.05  
460 reflectance units for the color and black standards, and to within 0.01 for the grayscale standards,  
461 in all geometries except for the highest phase angles (Figures 22-23 and Figures S8-S9).  
462 Wavelengths near 1100 nm and 1300 nm typically have large residuals (e.g., Figure 23 gray),  
463 which we attribute to known polarization artifacts that are prominent in the data from Buz et al.  
464 but nearly absent in TANAGER spectra (see Text S5). We also observe structure in the residuals  
465 near 1900 nm (e.g., Figure 22), where there is an H<sub>2</sub>O absorption; Buz et al. (2019) note  
466 variations in this band strength in their spectra which they attribute to water in the instrument  
467 path length, and they recommend caution when interpreting small fluctuations in this region.

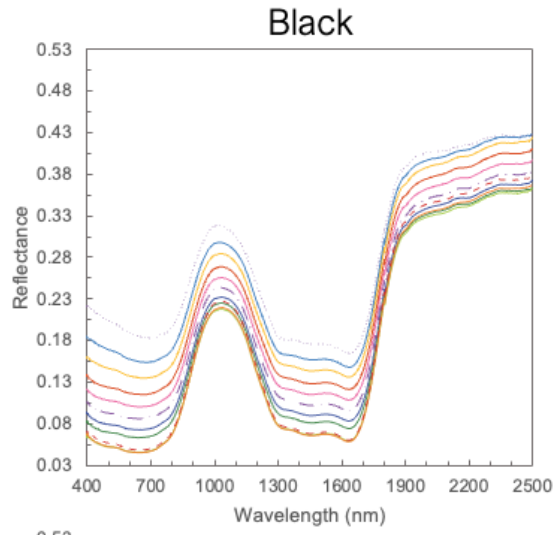
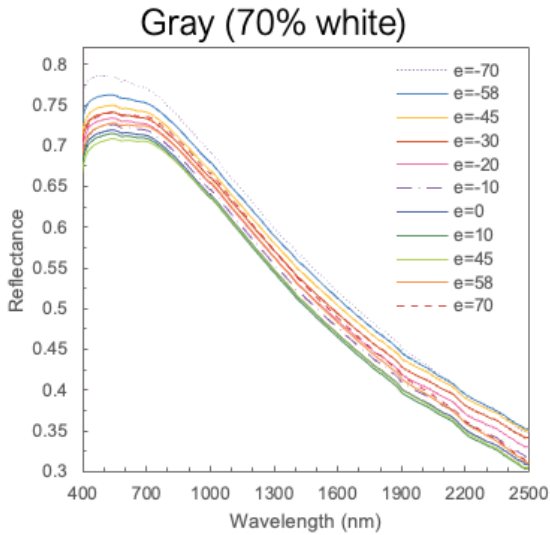
468 We observe the same general scattering behaviors for all targets as those reported by Buz  
469 et al. (2019): the brighter samples (light gray, red, cyan and yellow) are quasi-isotropic, the  
470 AluWhite sample is weakly backward scattering, and the darker samples (black, dark gray and  
471 green) are strongly forward-scattering. TANAGER spectra of the brighter samples suggest they  
472 are more isotropic than demonstrated by Buz et al. (2019) (i.e., TANAGER spectra show less  
473 variation in reflectance at high phase angles; Figure 22, Figure S8). The two highly forward-  
474 scattering geometries ( $i = 30^\circ$  and  $e = -58^\circ, -70^\circ$ ) show reversed behavior in TANAGER spectra  
475 compared to Buz et al. (2019); however, the TANAGER spectra are more consistent with the  
476 known scattering behaviors for these targets (e.g., the  $e = -70^\circ$  spectrum is higher reflectance than  
477 the  $e = -58^\circ$  spectrum for strongly forward-scattering targets; Figure 23, Figure S9). Therefore,  
478 the discrepancies between the two labs' datasets may indicate improvements in TANAGER  
479 spectra over the previously-published versions.



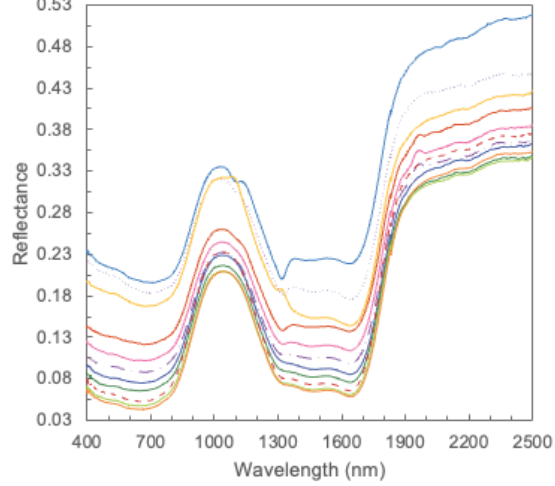
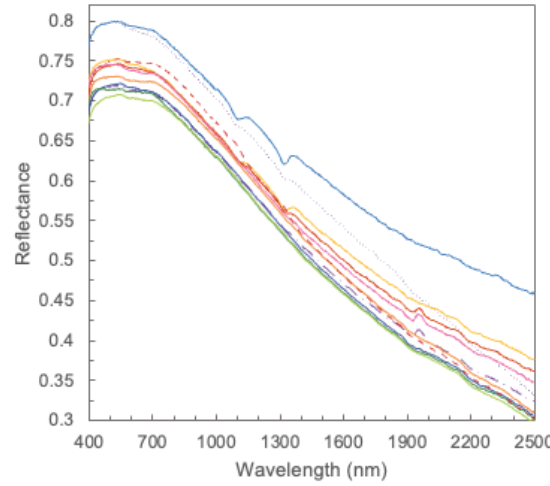
480

481 **Figure 22:** Spectra of the cyan and red Mastcam-Z caltarget witness samples at multiple viewing  
 482 geometries from TANAGER (top) compared to Buz et al. (2019) (middle), with residuals (bottom). All  
 483 measurements were acquired at  $i = 30^\circ$  and  $az = 0^\circ$ .

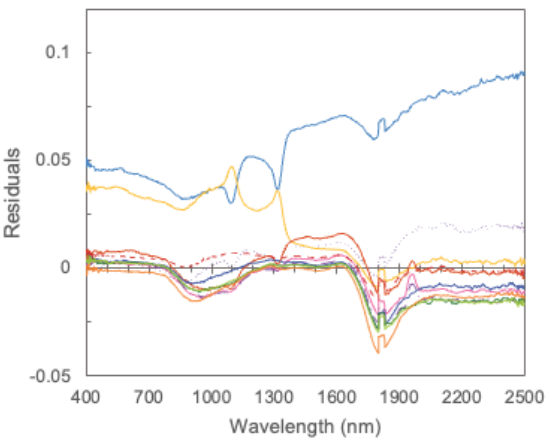
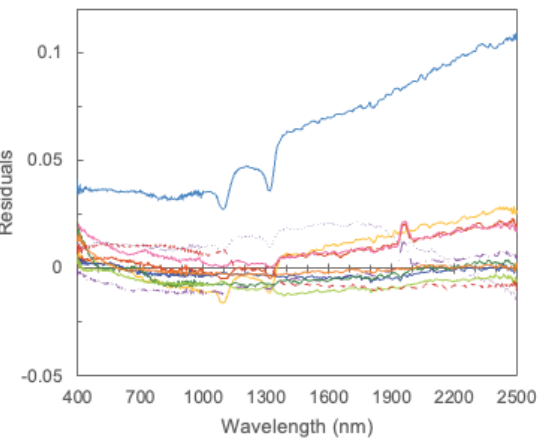
TANAGER Run 1, 2022



Buz et al., 2019



Buz et al. - TANAGER



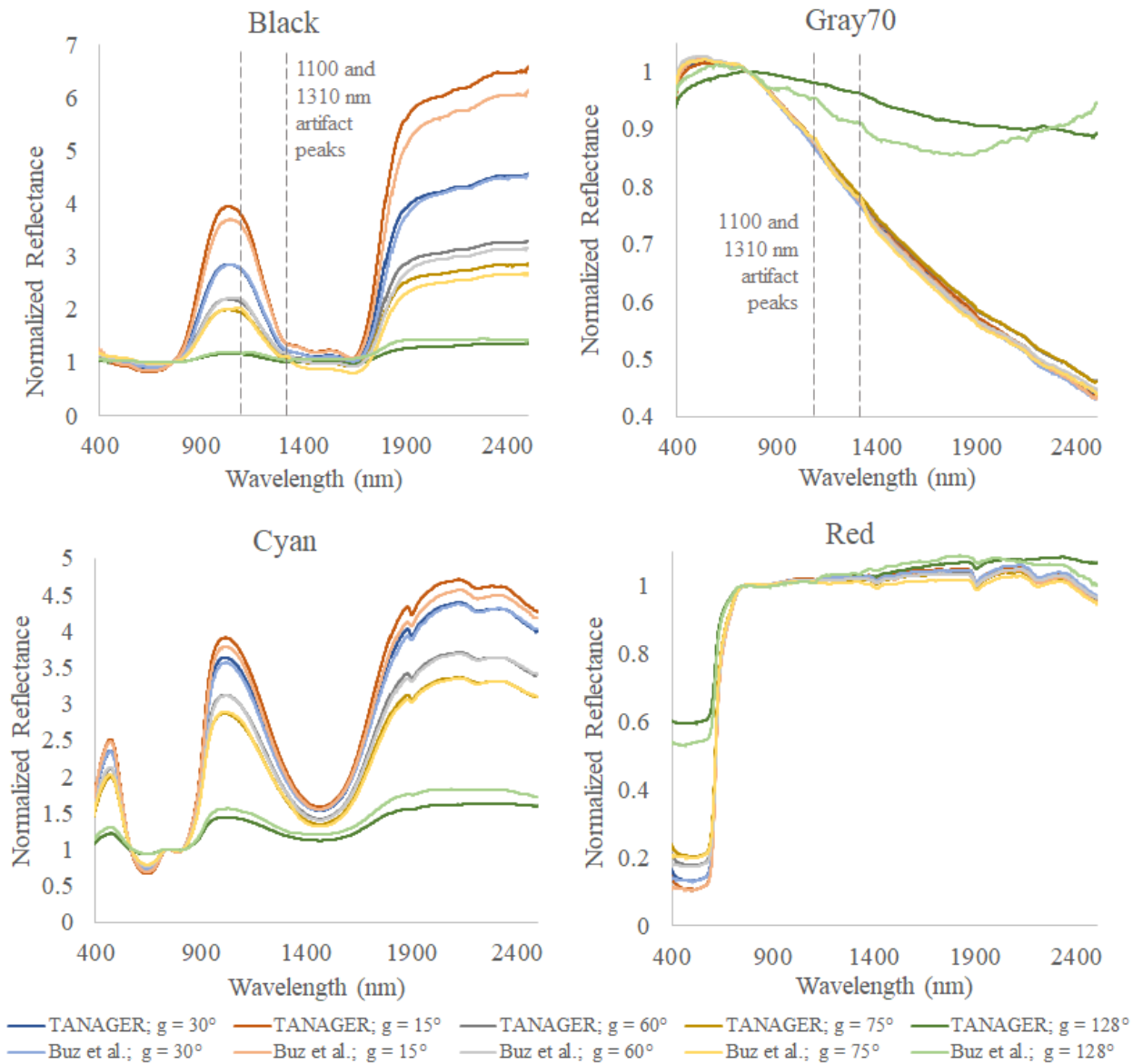
484

485 **Figure 23:** Spectra of the light gray (70% white) and black Mastcam-Z caltarget witness samples at  
 486 multiple viewing geometries from TANAGER (top) compared to Buz et al. (2019) (middle), with residuals  
 487 (bottom). All measurements were acquired at  $i = 30^\circ$  and  $az = 0^\circ$ .

488

489 To minimize differences in absolute reflectance and focus on differences in spectral  
490 shape, we also normalized spectra to 1.0 at 754 nm and calculated relative RMSE at a  
491 representative range of geometries. The normalized spectra (Figure 24) have only minor  
492 differences in spectral shape and slope (except for the light gray target at  $g = 128^\circ$ ). Relative  
493 RMSE values (Table 3) are less than 5% with two exceptions: (1) the black target and (2) highly  
494 forward-scattering geometries. We attribute the black target's high relative RMSE to its dark  
495 albedo and low signal-to-noise, so we do not find these values concerning, but recommend  
496 caution when interpreting subtle spectral shapes in TANAGER spectra of dark materials.

497 The high relative RMSE values for the very forward-scattering geometry ( $g = 128^\circ$ ) may  
498 result from differences between the Buz et al. (2019) and TANAGER lab setups. At the highest  
499 measurable phase angles, it is possible that TANATER's detector may receive stray light  
500 reflected from lab walls and cabinets at high emission angles. To test and potentially mitigate  
501 scattered light effects, we hung blackout curtains on the surfaces immediately adjacent to  
502 TANAGER (shown in Figure 13) and recollected the  $g = 128^\circ$  spectra, which led to general  
503 decreases in overall reflectance (Figure S10) and improvements in relative RMSE values (Table  
504 3). We now hang black curtains over all surfaces adjacent to TANAGER as part of our standard  
505 procedure.



506

507 **Figure 24:** Spectra normalized to 754 nm of select caltargets from TANAGER (darker lines) and Buz et  
 508 al. (2019) (lighter lines) at a range of viewing geometries. Minor artifact peaks are marked in the Gray70  
 509 and Black Buz et al. (2019) spectra for  $g = 75^\circ$  and  $g = 128^\circ$ .

510

	$g = 15^\circ$	$g = 30^\circ$	$g = 60^\circ$	$g = 75^\circ$	$g = 128^\circ$	$g = 128^\circ$ (with black curtains)
Cyan	3.9%	1.9%	1.2%	1.3%	9.0%	4.4%
Green	4.3%	1.9%	2.0%	2.2%	8.0%	4.1%
Red	1.9%	1.3%	1.4%	1.8%	2.8%	2.9%
Yellow	1.6%	1.3%	1.4%	1.7%	3.6%	4.6%

Gray33	0.7%	1.5%	2.7%	3.4%	4.3%	3.8%
Gray70	0.9%	0.9%	1.7%	2.6%	4.2%	3.7%
Black	9.7%	3.5%	5.6%	7.9%	6.7%	5.9%
AluWhite	0.0%	0.0%	0.0%	0.0%	0.0%	0.0%

511 **Table 3:** Relative RMSE comparing spectra normalized to 754 nm from Buz et al. (2019) and TANAGER  
512 at a range of geometries for cross calibration. Green squares have RMSE <1%, yellow-green between  
513 1% and 3% RMSE, orange between 3% and 5% RMSE, and red above 5%. “Blackout” RMSE, right,  
514 compares Buz et al. (2019) spectra to TANAGER data collected with the addition of blackout curtains in  
515 the laboratory.

516

#### 517 4.2 Repeatability

518 The repeatability of TANAGER spectra was assessed through multiple measurements of  
519 the caltarget materials at the geometries specified in Buz et al. (2019): we compared two sets of  
520 spectra collected with TANAGER in November 2022 and February 2023. The gray and black  
521 targets have residuals < 0.01 reflectance units for all spectra except at the largest phase angles,  
522 and color target spectra are generally repeatable to within 0.02 reflectance units (Figures S11-  
523 S14). To assess repeatability of spectral shapes (as opposed to absolute reflectance), we also  
524 normalized the spectra to 1.0 at 754 nm to calculate relative RMSE (as in Section 4.1). All  
525 target-geometry combinations fall well below our 5% relative RMSE threshold, with 29 of 35  
526 target-geometry combinations below 1% RMSE (Table 4). The very forward scattering geometry  
527 is less consistent than other geometries, but overall the data show remarkable reproducibility.

	$g = 15^\circ$	$g = 30^\circ$	$g = 60^\circ$	$g = 75^\circ$	$g = 128^\circ$
Cyan	0.4%	1.0%	0.7%	1.1%	3.5%
Green	0.4%	0.9%	0.6%	1.1%	4.2%
Red	0.3%	0.4%	0.8%	0.8%	1.1%
Yellow	0.3%	0.8%	0.7%	0.7%	2.1%
Gray33	0.2%	0.3%	0.2%	0.3%	0.9%
Gray70	0.3%	0.4%	0.5%	0.5%	0.5%

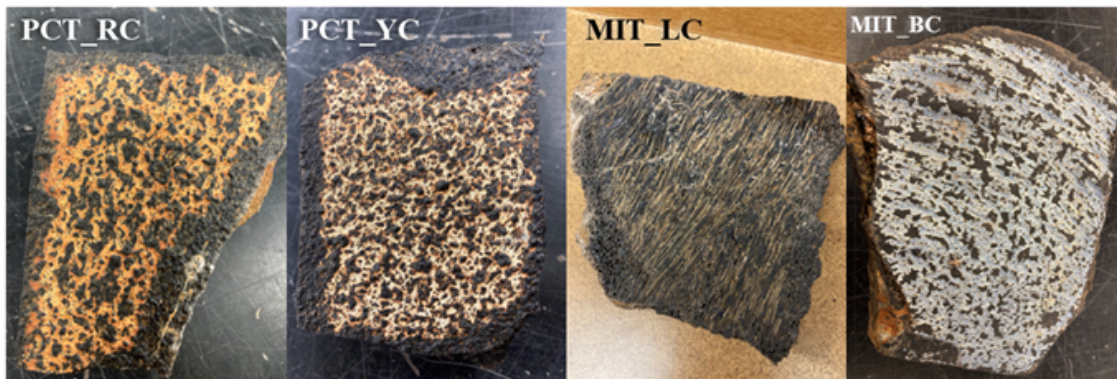
Black	0.8%	2.0%	1.0%	1.2%	0.4%
AluWhite	0.6%	0.5%	0.5%	0.5%	1.1%

528  
529  
530  
531  
532

**Table 4:** Relative RMSE comparing duplicate runs on TANAGER normalized to 754 nm for the Caltargets at a range of geometries. Green squares have RMSE <1%, yellow-green between 1% and 3% RMSE, and orange between 3% and 5% RMSE.

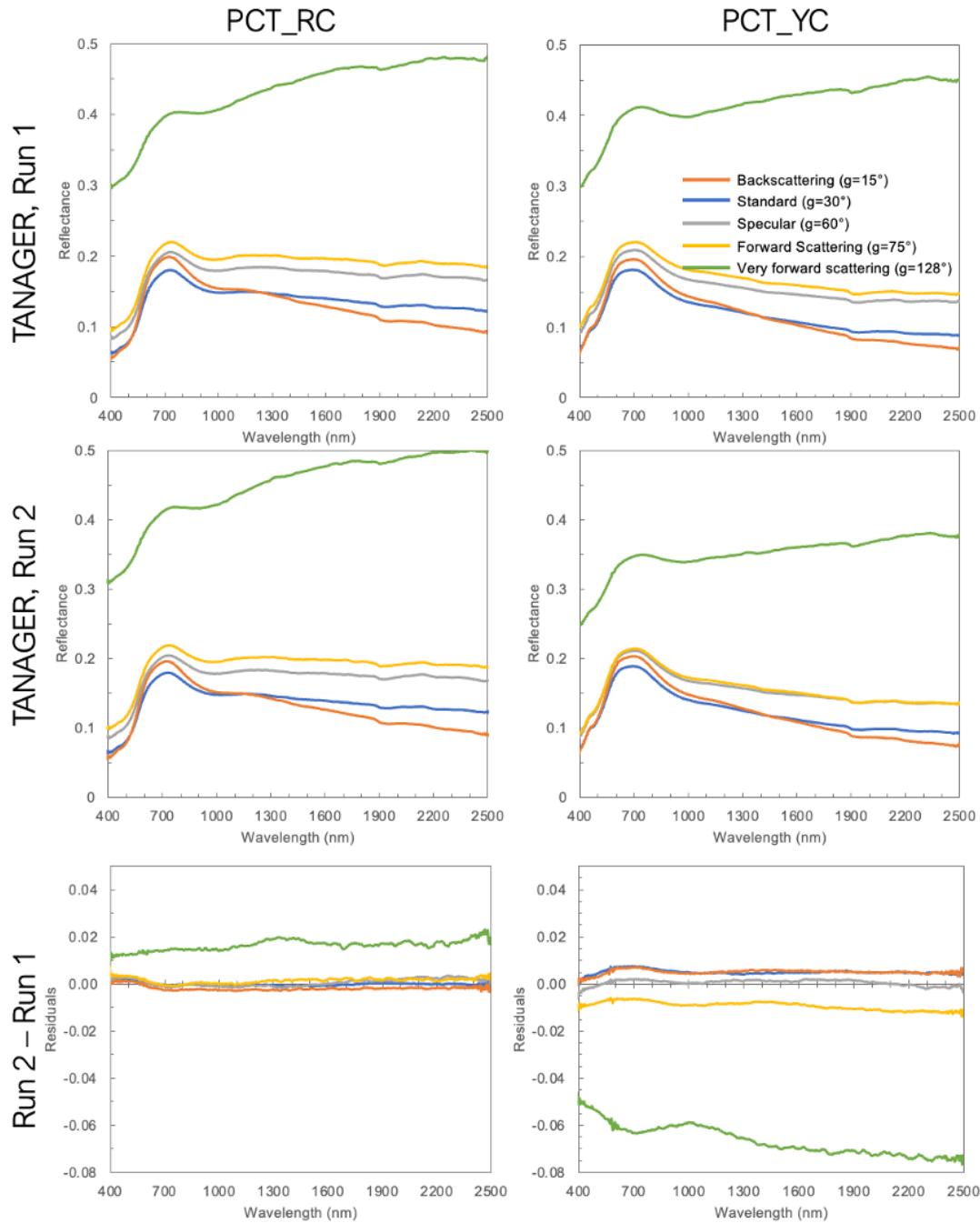
533  
534  
535  
536  
537  
538  
539

To test repeatability of spectral measurements of heterogeneous, geologic surfaces, we collected duplicate spectra at a range of phase angles from a set of four naturally-coated basalt samples from Hawaii Volcanoes National Park. All samples were collected from the Puna Coast and Mauna Iki Trails (Theuer et al., 2024) and all have brightly-colored coatings in a mottled pattern, except for MIT\_LC, which has a more uniform reflective and chatoyant coating over fine-scaled flow textures (Figure 25). We documented the placement and orientation of each sample, which we referenced while resetting samples between the first and second set of spectra.



540  
541  
542  
543

**Figure 25:** Heterogeneous, naturally-coated basalts samples used to test TANAGER's measurement repeatability.



544  
 545 **Figure 26:** Spectra of heterogeneous, naturally-coated basalt samples (PCT\_RC and PCT\_YC, see  
 546 Figure 25) from two TANAGER data collection runs (top and middle) with residuals (bottom). All  
 547 measurements were acquired at  $i = 30^\circ$  and  $az = 0^\circ$ .  
 548

549 Data from the two runs reproduce the same spectral shapes and scattering behaviors: the  
 550 samples are highly forward-scattering, with substantially higher reflectances and more positive  
 551 near-infrared slopes at  $g = 128^\circ$  (Figure 26, Figure S15). For absolute reflectance spectra,

552 residuals for most geometries are  $< 0.005$  reflectance units. For spectra normalized to 1.0 at 754  
 553 nm, the two datasets have a relative RMSE of 3% or below (Table 9). The one exception is for  
 554 the dark sample MIT\_LC in the backscattering geometry, which has very low reflectance values  
 555 (Figure S15). The reproducibility of TANAGER spectra for these samples gives us confidence in  
 556 the consistency of both the spectrogoniometer’s performance and our sample staging procedure.  
 557

	$g = 15^\circ$	$g = 30^\circ$	$g = 60^\circ$	$g = 75^\circ$	$g = 128^\circ$
PCT_RC	0.6%	0.4%	1.0%	1.1%	0.4%
PCT_YC	1.5%	1.0%	1.1%	3.0%	1.1%
MIT_LC	5.6%	2.3%	2.1%	3.0%	2.1%
MIT_BC_2	2.1%	2.9%	2.2%	2.8%	0.6%

558  
 559 **Table 9:** Relative RMSE comparing duplicate runs on TANAGER normalized to 754 nm for four coated  
 560 basalt surfaces at a range of geometries. Green squares have RMSE  $< 1\%$ , yellow-green between 1% and  
 561 3% RMSE, orange between 3% and 5% RMSE, and red  $> 5\%$  RMSE.  
 562

## 563 5. Science Applications and Data Sharing

564 Our preliminary science analyses have utilized TANAGER’s unique design for rapid  
 565 spectral measurements for large suites of natural rock surfaces, either at a single “standard”  
 566 geometry (Rice et al., 2023) or over the full scattering hemisphere (Curtis, 2022; Theuer et al.,  
 567 2024). Other initial studies include characterizations of multi-phase mineral mixtures (Lapo et  
 568 al., 2023) and synthetic rock coatings on slabs (Gabbert et al., 2023) and sands (Gabbert et al.,  
 569 2024). Because TANAGER’s sample tray also accommodates SEM-mounted samples, we can  
 570 easily correlate spectrogoniometric measurements with microtextural properties from  
 571 backscattered electron (BSE) images and surface topography measurements (Duflot et al., 2022).

572 Ongoing work in the WWU Mars Lab will continue to exploit TANAGER’s capabilities  
 573 for interrogating natural rock surfaces. More generally, we anticipate that TANAGER’s design  
 574 can be useful for a variety of investigations, such as determining the bidirectional reflectance

575 distribution function (BRDF) and deriving optical constants of minerals (e.g., Lucy, 1998; Sklute  
576 et al., 2015). We hope other laboratories will adapt TANAGER's open-source design (Hoza et  
577 al., 2023) and software (Hoza, 2023) for their own niche analyses (see Data Availability  
578 Statement).

579         When spectral datasets from TANAGER are published in peer-reviewed studies, we will  
580 make them available via VISOR (the [V]isible and [I]nfrared [S]pectroscopy br[o]wse[r],  
581 <https://westernreflectancelab.com/visor/>), an online data sharing and spectra visualization tool  
582 developed by Million Concepts, LLC in partnership with the WWU Mars Lab (Million et al.,  
583 2022). VISOR allows users to search for spectra from TANAGER and/or other published  
584 spectral databases, download spectra with associated metadata (viewing geometry and sample  
585 information), and dynamically plot user-selected spectra. Plotting capabilities include adjusting  
586 axes, normalizing spectra, applying offsets, measuring selected band depths and other spectral  
587 parameters, and convolving to the bandpasses of spacecraft multispectral cameras. We will also  
588 archive all published TANAGER datasets via third party repositories (e.g., <https://zenodo.org/> or  
589 <https://cedar.wvu.edu/>) with a digital object identifier (DOI) and persistent identifier link.

590

## 591 **6. Conclusions**

592         TANAGER is a custom spectrogoniometer which is fully automated and integrated with  
593 a Malvern PanAnalytical ASD FieldSpec4 Hi-Res reflectance spectrometer. We defined  
594 TANAGER's performance requirements to enable rapid, automated spectral data collection  
595 across the full scattering hemisphere for multiple, bulky rock samples with natural surfaces. In a  
596 detailed characterization of TANAGER's performance, all defined requirements have been met.  
597 We reevaluated a selection of the performance sub-requirements after ~300 hours of use and

598 found only minor changes to the system; we recommend frequent monitoring of some  
599 components, including laser guides and sample tray motors.

600       Using well-characterized color calibration targets, we have validated the accuracy of  
601 TANAGER spectra in comparison to published data. TANAGER spectra match those published  
602 from other spectrogoniometers within 5% relative RMSE, except for very low-albedo targets. In  
603 repeated TANAGER data collection runs for the same samples, we confirm that TANAGER  
604 spectra are self-consistent to within 2% in almost all instances. We also confirm that the system  
605 introduces no discernable noise or artifacts; in fact, TANAGER improves the polarization  
606 artifacts from ~1000 nm to 1400 nm that commonly occur in FieldSpec data at high phase  
607 angles. Furthermore, we find that TANGER's light source causes only minimal sample heating  
608 (+2 to 4°C over typical exposure durations) and is highly unlikely to influence sample properties  
609 such as hydration state.

610       The advantages of TANAGER's unique design include automation for rapid data  
611 acquisition, highly customizable viewing geometries, accommodation of multiple and/or  
612 bulky/irregular samples, and easy transfer to SEM for correlation with surface textural and  
613 compositional properties. For our near-term science analyses, TANAGER will primarily be used  
614 to characterize the surfaces of naturally-weathered rocks as analogs to the martian surface;  
615 however, TANAGER can be utilized for a variety of applications in reflectance spectroscopy.  
616 We encourage other investigators to use and/or modify TANAGER's open-source design and  
617 software for their laboratories' needs.

618

619 **Acknowledgements**

620 This work was funded as part of a NASA Solar System Working Program grant. We  
621 thank the staff of First Mode, LLC for their support in all stages of this project, including Peter  
622 Illsley, Elizabeth Frank and Sophia Kim. Western Washington University’s College of Science  
623 and Engineering, Geology Department, and Machine Shop supported laboratory renovations to  
624 accommodate TANAGER. We also thank Chase Million and Michael St. Clair of Million  
625 Concepts, LLC for development and ongoing support of VISOR for data sharing. Finally, we  
626 thank the Mastcam-Z instrument team for use of the caltarget witness samples.

627

628 **Data Availability Statement**

629 TANAGER’s computer-aided design (CAD), electrical schematics, and bill of materials  
630 (BOM) are publicly available as Hoza et al. (2023). TANAGER’s custom software (“tanager-  
631 feeder”), which commands its motors, interfaces with the spectrometer, and visualizes the data,  
632 is open-source and available as Hoza (2023). All spectral data acquired for TANAGER’s  
633 validation and characterization are available as Lapo et al. (2024).

634

635 **References**

- 636 Allan, A. (2011). *Basic Sensors in IOS: Programming the Accelerometer, Gyroscope, and*  
637 *More*. O’Reilly Media, Inc.
- 638 ASD Inc. (2017, September). *FieldSpec4 User Guide*.
- 639 J.F. Bell III, J. Joseph, J.N. Sohl-Dickstein, H.M. Arneson, M.J. Johnson, M.T. Lemmon, &  
640 D. Savransky, In-flight calibration and performance of the Mars Exploration Rover  
641 Panoramic Camera (Pancam) Instruments. *J. Geophys. Res.* 111, E02S03 (2006b).  
642 <https://doi.org/10.1029/2005JE002444>
- 643 J.F. Bell III, A. Godber, S. McNair, M.C. Caplinger, J.N. Maki, M.T. Lemmon, et al., The  
644 Mars Science Laboratory Curiosity rover Mast Camera (Mastcam) instruments: pre-

- 645 flight and in-flight calibration, validation, and data archiving. *Earth Space Sci.* 4, 396–  
646 452 (2017). <https://doi.org/10.1002/2016EA000219>
- 647 Bhandari, A., Hamre, B., Frette, Ø., Zhao, L., Stamnes, J. J., & Kildemo, M. (2011).  
648 Bidirectional reflectance distribution function of Spectralon white reflectance standard  
649 illuminated by incoherent unpolarized and plane-polarized light. *Applied Optics*,  
650 50(16), 2431–2442. <https://doi.org/10.1364/AO.50.002431>
- 651 Biliouris, D., Verstraeten, W. W., Dutré, P., Van Aardt, J. A. N., Muys, B., & Coppin, P.  
652 (2007). A Compact Laboratory Spectro-Goniometer (CLabSpeG) to Assess the BRDF  
653 of Materials. Presentation, Calibration and Implementation on *Fagus sylvatica* L.  
654 Leaves. *Sensors*, 7(9), 1846–1870. <https://doi.org/10.3390/s7091846>
- 655 Bishop, J. L., III, J. F. B., & Moersch, J. E. (Eds.). (2020). *Remote Compositional Analysis:  
656 Techniques for Understanding Spectroscopy, Mineralogy, and Geochemistry of  
657 Planetary Surfaces*. Cambridge, UK: Cambridge University Press.  
658 <https://doi.org/10.1017/9781316888872>
- 659 Buz, J., Ehlmann, B. L., Kinch, K., Madsen, M. B., Johnson, J. R., Rice, M. S., et al. (2019).  
660 Photometric characterization of Lucideon and Avian Technologies color standards  
661 including application for calibration of the Mastcam-Z instrument on the Mars 2020  
662 rover. *Optical Engineering*, 58(02), 027108. <https://doi.org/10.1117/1.OE.58.2.027108>
- 663 Camon, A., & Lemelin, M. (2024). Characterizing the Spectra of Ilminite, Hematite, Mg-  
664 Spinel and Regolith Simulants to Prepare for Upcoming Lunar Missions (Vol. 55, p.  
665 Abstract 1979). Presented at the Lunar and Planetary Science Conference. Retrieved  
666 from <https://www.hou.usra.edu/meetings/lpsc2024/pdf/1979.pdf>
- 667 Clark, B. E., Helfenstein, P., Bell, J. F., Peterson, C., Veverka, J., Izenberg, N. I., et al.  
668 (2002). NEAR Infrared Spectrometer Photometry of Asteroid 433 Eros. *Icarus*, 155(1),  
669 189–204. <https://doi.org/10.1006/icar.2001.6748>
- 670 Clark, R. N., & Roush, T. L. (1984). Reflectance spectroscopy: Quantitative analysis  
671 techniques for remote sensing applications. *Journal of Geophysical Research: Solid  
672 Earth*, 89(B7), 6329–6340. <https://doi.org/10.1029/JB089iB07p06329>
- 673 Clark, R. N. (1999). Remote Sensing for the Earth Sciences. In A. N. Rencz (Ed.), *Manual  
674 of Remote Sensing* (3rd ed., Vol. 3, pp. 3–55). John Wiley and Sons, Inc.
- 675 Cloutis, E. A., Craig, M. A., Kruzelecky, R. V., Jamroz, W. R., Scott, A., Hawthorne, F. C.,  
676 & Mertzman, S. A. (2008). Spectral reflectance properties of minerals exposed to  
677 simulated Mars surface conditions. *Icarus*, 195(1), 140–168.
- 678 Curtis, S. (2022). Spectral variability in naturally weathered rock surfaces and implications  
679 for Mars (unpublished master's dissertation). WWU Graduate School Collection 1118.  
680 Retrieved from <https://cedar.wvu.edu/wwuet/1118>
- 681 Dufлот, S. A., Kraft, M. D., Rice, M. S., Curtis, S. A., & Lapo, K. E. (2022). Quantitative  
682 Characterization of Weathered Rock Surface Textures and Effects on VNIR

- 683 Spectrogoniometry (Vol. 53, Abstract 2368). Presented at the Lunar and Planetary  
684 Science Conference. Retrieved from  
685 <https://www.hou.usra.edu/meetings/lpsc2022/pdf/2368.pdf>
- 686 Fernando, J., Schmidt, F., Pilorget, C., Pinet, P., Ceamanos, X., Douté, S., et al. (2015).  
687 Characterization and mapping of surface physical properties of Mars from CRISM  
688 multi-angular data: Application to Gusev Crater and Meridiani Planum. *Icarus*, 253,  
689 271–295. <https://doi.org/10.1016/j.icarus.2015.03.012>
- 690 Gabbert, M. D. V., Rice, M. S., Kraft, M. D., & Lapo, K. E. (2023). Visible to Near-  
691 Infrared Spectroscopy and Photometry of Synthetic Coatings on Ultramafic Rocks with  
692 Applications for Mars. (Vol. 54, Abstract 2390). Presented at the Lunar and Planetary  
693 Science Conference. Retrieved from  
694 <https://www.hou.usra.edu/meetings/lpsc2023/pdf/2390.pdf>
- 695 Gabbert, M. D. V., Rice, M. S., Kraft, M. D., & Lapo, K. E. (2024). Synthetic Coatings on  
696 Ultramafic Sands with Variable Angularities: Visible to Near-Infrared Spectroscopy  
697 and Applications to Jezero Crater, Mars (Vol. 55, Abstract 1788). Presented at the  
698 Lunar and Planetary Science Conference. Retrieved from  
699 <https://www.hou.usra.edu/meetings/lpsc2024/pdf/1788.pdf>
- 700 Guinness, E. A., Arvidson, R. E., Clark, I. H. D., & Shepard, M. K. (1997). Optical  
701 scattering properties of terrestrial varnished basalts compared with rocks and soils at the  
702 Viking Lander sites. *Journal of Geophysical Research: Planets*, 102(E12), 28687–  
703 28703. <https://doi.org/10.1029/97JE03018>
- 704 Hapke, B. (1993). *Theory of Reflectance and Emittance Spectroscopy* (2nd ed.). New York:  
705 Cambridge University Press.
- 706 Hayes, A. G., Corlies, P., Tate, C., Barrington, M., Bell, J. F., Maki, J. N., et al. (2021). Pre-  
707 Flight Calibration of the Mars 2020 Rover Mastcam Zoom (Mastcam-Z) Multispectral,  
708 Stereoscopic Imager. *Space Science Reviews*, 217(2), 29.  
709 <https://doi.org/10.1007/s11214-021-00795-x>
- 710 Hoza, K. (2019, June). Photometric investigations of weathering rinds and coatings with  
711 implications for Mars (M.S.). Western Washington University, Bellingham, WA.  
712 Retrieved from <https://cedar.wvu.edu/wwuet/921>
- 713 Hoza, K. (2023). *westernmarslab/tanager-feeder* (v1.0.0). Zenodo.  
714 <https://doi.org/10.5281/zenodo.8161157>
- 715 Hoza, K., Kim. Sophia, Illsley, P., & Karch, J. (2023). *westernmarslab/tanager-design*  
716 (v1.0.0). Zenodo. <https://doi.org/10.5281/zenodo.8161143>
- 717 Hoza, K. M., & Rice, M. S. (2019). An Automated Goniometer System for Reflectance  
718 Spectroscopy (Vol. 50, p. Abstract 2958). Presented at the Lunar and Planetary Science  
719 Conference. Retrieved from <https://www.hou.usra.edu/meetings/lpsc2019/pdf/2958.pdf>

- 720 Johnson, J. R., Kirk, R., Soderblom, L. A., Gaddis, L., Reid, R. J., Britt, D. T., et al. (1999).  
721 Preliminary results on photometric properties of materials at the Sagan Memorial  
722 Station, Mars. *Journal of Geophysical Research: Planets*, 104(E4), 8809–8830.  
723 <https://doi.org/10.1029/98JE02247>
- 724 Johnson, J. R., Grundy, W. M., Lemmon, M. T., Bell III, J. F., Johnson, M. J., Deen, R. G.,  
725 et al. (2006a). Spectrophotometric properties of materials observed by Pancam on the  
726 Mars Exploration Rovers: 1. Spirit. *Journal of Geophysical Research: Planets*, 111(E2).  
727 <https://doi.org/10.1029/2005JE002494>
- 728 Johnson, J. R., Grundy, W. M., Lemmon, M. T., Bell III, J. F., Johnson, M. J., Deen, R., et  
729 al. (2006b). Spectrophotometric properties of materials observed by Pancam on the  
730 Mars Exploration Rovers: 2. Opportunity. *Journal of Geophysical Research: Planets*,  
731 111(E12). <https://doi.org/10.1029/2006JE002762>
- 732 Johnson, J. R., Grundy, W. M., Lemmon, M. T., Liang, W., Bell, J. F., Hayes, A. G., &  
733 Deen, R. G. (2021). Spectrophotometric properties of materials observed by Pancam on  
734 the Mars Exploration Rovers: 4. Final mission observations. *Icarus*, 357, 114261.  
735 <https://doi.org/10.1016/j.icarus.2020.114261>
- 736 Johnson, J. R., Grundy, W. M., Lemmon, M. T., Liang, W., Bell, J. F., Hayes, A. G., &  
737 Deen, R. G. (2022). Spectrophotometric properties of materials from the Mars Science  
738 Laboratory at Gale crater: 1. Bradbury Landing to Cooperstown. *Planetary and Space  
739 Science*, 222, 105563. <https://doi.org/10.1016/j.pss.2022.105563>
- 740 K.M. Kinch, M.B. Madsen, J.F. Bell III., J.N. Maki, Z. Bailey, A.G. Hayes, et al. (2020),  
741 Radiometric calibration targets for the Mastcam-Z Camera on the Mars 2020 Rover  
742 mission. *Space Sci. Rev.* <https://doi.org/10.1007/s11214-020-00774-8>
- 743 Kharutskiy, D. (2014). *Vibration Analysis (Version 4)* [iPhone Application]. Retrieved from  
744 <https://apps.apple.com/us/app/vibration-analysis/id817385888>
- 745 Lapo, K. E. (2021, March 5). *Martian Spectroscopy: Laboratory calibration of the  
746 Perseverance rover's Mastcam-Z and photometric investigation of Mars-analog ferric-  
747 coated sand (M.S.)*. Western Washington University, Bellingham, WA. Retrieved from  
748 <https://cedar.wvu.edu/wwuet/1011>
- 749 Lapo K. E., Rice, M. S., Eng, A. M., & Curtis, S. A. (2023). VNIR Spectral Masking Effects  
750 of Hematite on Mafic Mars Analogs (Vol. 54, Abstract 1746). Presented at the Lunar  
751 and Planetary Science Conference. Retrieved from  
752 <https://www.hou.usra.edu/meetings/lpsc2023/pdf/1746.pdf>
- 753 Lapo, K. E., Hoza, K., Theuer, S. & Rice, M. S. (2024). Reflectance spectroscopy datasets  
754 for the validation of TANAGER. *Geology Faculty Publications*, 107.  
755 <https://doi.org/10.25710/qzzg-bp63>
- 756 Lévesque, M. P., & Dissanska, M. (2016). Field spectrometer measurement errors in  
757 presence of partially polarized light; evaluation of ground truth measurement accuracy.  
758 *Optics Express*, 24(24), 27199. <https://doi.org/10.1364/OE.24.027199>

- 759 Lichtenberg, K. A., Arvidson, R. E., Poulet, F., Morris, R. V., Knudson, A., Bell, J. F., et al.  
760 (2007). Coordinated analyses of orbital and Spirit Rover data to characterize surface  
761 materials on the cratered plains of Gusev Crater, Mars. *Journal of Geophysical*  
762 *Research: Planets*, 112(E12). <https://doi.org/10.1029/2006JE002850>
- 763 Lucey, P. G. (1998). Model near-infrared optical constants of olivine and pyroxene as a  
764 function of iron content. *Journal of Geophysical Research*, 103(E1), 1703–1713.  
765 <https://doi.org/10.1029/97JE03145>
- 766 Million, C. C., St. Clair, M., Rice, M. S., & Vaughan, A. (2022). Software Tools for Rapid  
767 Analysis of Mastcam-Z Multispectral Data (Vol. 53, Abstract 2533). Presented at the  
768 Lunar and Planetary Science Conference. Retrieved from  
769 <http://www.hou.usra.edu/meetings/lpsc2022/pdf/2533.pdf>
- 770 Painter, T., Paden, B., & Dozier, J. (2003). Automated spectro-goniometer: A spherical  
771 robot for the field measurement of the directional reflectance of snow. *Review of*  
772 *Scientific Instruments*, 74(12), 5179–5188. <https://doi.org/10.1063/1.1626011>
- 773 Pilorget, C., Fernando, J., Ehlmann, B. L., Schmidt, F., & Hiroi, T. (2016). Wavelength  
774 dependence of scattering properties in the VIS–NIR and links with grain-scale physical  
775 and compositional properties. *Icarus*, 267, 296–314.  
776 <https://doi.org/10.1016/j.icarus.2015.12.029>
- 777 Pommerol, A., Thomas, N., Jost, B., Beck, P., Okubo, C., & McEwen, A. S. (2013).  
778 Photometric properties of Mars soils analogs. *Journal of Geophysical Research: Planets*,  
779 118(10), 2045–2072. <https://doi.org/10.1002/jgre.20158>
- 780 Potin, S., Brissaud, O., Beck, P., Schmitt, B., Magnard, Y., Correia, J.-J., et al. (2018).  
781 SHADOWS: a spectro-gonio radiometer for bidirectional reflectance studies of dark  
782 meteorites and terrestrial analogs: design, calibrations, and performances on  
783 challenging surfaces. *Applied Optics*, 57(28), 8279–8296.  
784 <https://doi.org/10.1364/AO.57.008279>
- 785 Rice, M. S., Johnson, J. R., Million, C. C., St. Clair, M., Horgan, B. N., Vaughan, A., et al.  
786 (2023). Spectral variability of rocks and soils on the Jezero crater floor: A summary of  
787 multispectral observations from Perseverance’s Mastcam-Z instrument. *Journal of*  
788 *Geophysical Research: Planets*, 128(10), e2022JE007548.  
789 <https://doi.org/10.1029/2022JE007548>
- 790 Schmidt, F., & Fernando, J. (2015). Realistic uncertainties on Hapke model parameters from  
791 photometric measurement. *Icarus*, 260, 73–93.  
792 <https://doi.org/10.1016/j.icarus.2015.07.002>
- 793 Schröder, S. E., & Keller, H. U. (2009). The unusual phase curve of Titan’s surface  
794 observed by Huygens’ Descent Imager/Spectral Radiometer. *Planetary and Space*  
795 *Science*, 57, 1963–1974. <https://doi.org/10.1016/j.pss.2009.03.012>
- 796 Shaw, A., Daly, M. G., Cloutis, E., Basic, G., Hamilton, D., Tait, K., et al. (2016).  
797 Reflectance properties of grey-scale Spectralon® as a function of viewing angle,

- 798 wavelength, and polarization. *International Journal of Remote Sensing*, 37(11), 2510–  
799 2523. <https://doi.org/10.1080/01431161.2016.1182664>
- 800 Shepard, M. K. (2017). *Introduction to Planetary Photometry*. Cambridge: Cambridge  
801 University Press. <https://doi.org/10.1017/9781316443545>
- 802 Shepard, M. K., & Arvidson, R. E. (1999). The Opposition Surge and Photopolarimetry of  
803 Fresh and Coated Basalts, *Icarus*, 10.1006/icar.1999.6150, 141, 1, (172-178).
- 804 Shepard, M. K., & Helfenstein, P. (2007). A test of the Hapke photometric model. *Journal of*  
805 *Geophysical Research: Planets*, 112(E3). <https://doi.org/10.1029/2005JE002625>
- 806 Shkuratov, Y., Starukhina, L., Hoffmann, H., & Arnold, G. (1999). A Model of Spectral  
807 Albedo of Particulate Surfaces: Implications for Optical Properties of the Moon. *Icarus*,  
808 137(2), 235–246. <https://doi.org/10.1006/icar.1998.6035>
- 809 Sklute, E. C., Glotch, T. D., Piatek, J. L., Woerner, W. R., Martone, A. A., & Kraner, M. L.  
810 (2015). Optical constants of synthetic potassium, sodium, and hydronium jarosite.  
811 *American Mineralogist*, 100(5–6), 1110–1122. <https://doi.org/10.2138/am-2015-4824>
- 812 Stack, K. M., & Milliken, R. E. (2015). Modeling near-infrared reflectance spectra of clay  
813 and sulfate mixtures and implications for Mars. *Icarus*, 250, 332–356.  
814 <https://doi.org/10.1016/j.icarus.2014.12.009>
- 815 Theuer, S. A., Rice, M. S., Kraft, M. D., Mulcahy, S. R., Lapo, K. E., Garczynski, B. et al.  
816 (2024). Characterization and the Spectral and Photometric Behavior of Mars Analog  
817 Coated Hawaiian Basalt (Vol. 55, Abstract 2546). Presented at the Lunar and Planetary  
818 Science Conference. Retrieved from  
819 <https://www.hou.usra.edu/meetings/lpsc2024/pdf/2546.pdf>
- 820 Veverka, J., Helfenstein, P., Hapke, B., & Goguen, J. (1989). Photometry and polarimetry of  
821 Mercury. In *Mercury* (pp. 37–58). University of Arizona Press.  
822 <https://doi.org/10.2307/j.ctv1v090nx.7>